# Rotating horizontal convection

Roy Barkan<sup>1,†</sup>, Kraig B. Winters<sup>1,2</sup> and Stefan G. Llewellyn Smith<sup>2</sup>

Scripps Institution of Oceanography, UCSD, 9500 Gilman Drive, La Jolla CA 92093-0209, USA
 Department of Mechanical and Aerospace Engineering, Jacobs School of Engineering, UCSD, 9500 Gilman Drive, La Jolla CA 92093-0411, USA

(Received 24 July 2012; revised 25 February 2013; accepted 3 March 2013)

'Horizontal convection' (HC) is the generic name for the flow resulting from a buoyancy variation imposed along a horizontal boundary of a fluid. We study the effects of rotation on three-dimensional HC numerically in two stages: first, when baroclinic instability is suppressed and, second, when it ensues and baroclinic eddies are formed. We concentrate on changes to the thickness of the near-surface boundary layer, the stratification at depth, the overturning circulation and the flow energetics during each of these stages. Our results show that, for moderate flux Rayleigh numbers  $(O(10^{11}))$ , rapid rotation greatly alters the steady-state solution of HC. When the flow is constrained to be uniform in the transverse direction, rapidly rotating solutions do not support a boundary layer, exhibit weaker overturning circulation and greater stratification at all depths. In this case, diffusion is the dominant mechanism for lateral buoyancy flux and the consequent buildup of available potential energy leads to baroclinically unstable solutions. When these rapidly rotating flows are perturbed, baroclinic instability develops and baroclinic eddies dominate both the lateral and vertical buoyancy fluxes. The resulting statistically steady solution supports a boundary layer, larger values of deep stratification and multiple overturning cells compared with non-rotating HC. A transformed Eulerian-mean approach shows that the residual circulation is dominated by the quasi-geostrophic eddy streamfunction and that the eddy buoyancy flux has a non-negligible interior diabatic component. The kinetic and available potential energies are greater than in the non-rotating case and the mixing efficiency drops from  $\sim 0.7$  to  $\sim 0.17$ . The eddies play an important role in the formation of the thermal boundary layer and, together with the negatively buoyant plume, help establish deep stratification. These baroclinically active solutions have characteristics of geostrophic turbulence.

**Key words:** convection, geostrophic turbulence, ocean processes

#### 1. Introduction

Horizontal convection (HC) is the term used to describe the flow resulting from a buoyancy variation imposed along a horizontal boundary of a fluid (Stern 1975). In the ocean, the equator to pole gradient of solar irradiance produces differential surface buoyancy forcing, which is believed to play an important role in the large-scale

dynamics. HC is thus often used as simple model to study the large-scale overturning circulation, stratification and thermocline of the world oceans.

Based on a series of laboratory experiments and thermodynamic reasoning, Sandström (1908, 1916) speculated that a closed steady circulation can only be maintained if the stabilizing buoyancy source is located at a lower level than the destabilizing buoyancy source. This hypothesis, often referred to as Sandström's theorem, suggests that buoyancy forcing alone is an insufficient mechanism of supplying energy to the ocean circulation (Munk & Wunsch 1998). Jeffreys (1925) showed, however, that Sandström's argument was flawed because it ignored the effects of diffusion. Furthermore, Coman, Griffiths & Hughes (2006) revisited Sandström's experiment and found persistent circulation, even in cases where the stabilizing buoyancy source was located at the same level as, or above, the destabilizing source. Paparella & Young (2002) argued that HC is non-turbulent because in the limit that the kinematic viscosity  $\nu$  and diffusivity  $\kappa$  go to zero, for a fixed Prandtl number  $Pr \equiv \nu/\kappa$ , the volume-averaged kinetic energy dissipation goes to zero. This contrasts with typical turbulent flows for which the dissipation rate is set by the forcing at scales larger than those in the inertial subrange and is independent of the fluid viscosity. This argument, often referred to as the antiturbulence theorem, supports Sandström's hypothesis, suggesting that a hypothetical ocean circulation, driven by surface buoyancy forcing alone, could not exhibit the observed small-scale marine turbulence without other forms of energy sources. Recently, however, Scotti & White (2011) argued that the criterion leading to the antiturbulence theorem is too restrictive and that, based on certain statistical properties of the velocity gradient tensor which are common to all known turbulent flows, HC is in fact turbulent. In addition, using flow visualization techniques, Mullarney, Griffiths & Hughes (2004) and Stewart (2012) demonstrated in laboratory experiments of both heat- and salt-driven HC that the plume beneath the destabilizing buoyancy forcing is turbulent and suggested that it plays an important role in mixing the fluid.

Rossby (1965) performed a set of laboratory experiments of HC by differentially heating a fluid from below. Motivated by his observations at steady state, he derived scaling laws for the thermal boundary layer depth and the strength of the circulation (see § 3 for details). These scaling laws suggest that in the oceanic regime HC supports a thinner thermal boundary layer and weaker circulation and abyssal stratification than those observed (Munk & Wunsch 1998). These scaling laws have subsequently been verified by numerical simulations and laboratory experiments (Rossby 1998; Mullarney et al. 2004; Chiu-Webster, Hinch & Lister 2008; Ilicak & Vallis 2012). It thus seems that, although HC exhibits similar features to those observed in the overturning circulation of the oceans, additional physical processes and energy sources are important to obtain a better match with the oceanic regime. Previous numerical and laboratory studies have examined the effects of surface stress on HC (Beardsley & Festa 1972; Whitehead & Wang 2008; Tailleux & Rouleau 2010; Hazewinkel, Paparella & Young 2012; Ilicak & Vallis 2012). It was generally found that the addition of mechanical surface stress makes a substantial difference to the structure of the flow and to the stratification. Stewart (2012) examined the effects of mechanical stirring on HC in the laboratory. By parametrizing the effective turbulent diffusivity ( $\kappa_{eff}$ ) induced by the stirring rod in their experiments they found that stirring levels corresponding to  $\kappa_{eff} = 100\kappa$  ( $\kappa$  being the molecular diffusivity) are necessary for the stirring rod to dynamically dominate the effective turbulent diffusivity of the negatively buoyant plume.

In the present study, however, we are concerned primarily with the basic HC model and its applicability to oceanic processes. We suggest that in order to study HC in an oceanic context, rapid rotation has to be included and its effects understood. In nonrotating HC, the interior lateral buoyancy flux is accomplished via advection. When rapid rotation is added, one expects this lateral interior advective flux to be inhibited and for baroclinic instability to be generated, resulting in a very different pattern of circulation and buoyancy transport mechanism. We therefore focus our attention on the effects rotation has on HC and examine the nature of the resulting flow which we term 'rotating horizontal convection' (RHC). The importance of rotational effects on the ocean thermocline (corresponding to the thermal boundary layer in HC studies) is not a new concept and dates back to classical thermocline theory studies by Robinson & Stommel (1959), Bryan & Cox (1967), Welander (1971) and many others. Stern (1975) discusses specifically the thermal boundary layer scaling of HC in a rapidly rotating annulus. Hignett, Ibbetson & Killworth (1981) performed a set of laboratory experiments of RHC and describe the dynamics as being controlled by the parameter O defined as the square of the ratio of the non-rotating thermal-layer scale (Rossby boundary layer) to the viscous Ekman scale. Their experiments focused on the moderately rotating regime with  $O \sim O(1)$  and they proposed a similarity solution in the specific case of a quadratically varying surface temperature. They also discuss a critical value  $Q_c \approx 3.4$ , above which baroclinic instability sets in and waves are seen. Park & Whitehead (1999) performed a set of laboratory experiments of RHC in the moderately rotating regime and proposed scaling laws for the lateral heat flux and thermal boundary layer. They further showed that when typical North Atlantic values are introduced, their scaling law predicts heat flux values that are comparable to those observed if the diffusivity is taken as an 'eddy' diffusivity of 10<sup>-4</sup> m<sup>2</sup> s<sup>-1</sup>. We extend these studies by exploring the rapidly rotating regime,  $Q \gg 1$ , which is more relevant to the oceanic regime. We also allow for three-dimensional effects and the consequent generation of baroclinic eddies. Baroclinic eddies are thought to play an important role in the dynamics of the oceanic overturning circulation (Wolfe & Cessi 2010), the establishment of the ocean stratification (Marshall et al. 2002) and the transport of buoyancy and tracers in the ocean and the atmosphere (see Perez-Perez, Read & Moroz 2010 and references therein). The effects of eddies on large-scale flows are often illustrated using residual-mean theories based on the works of Andrews & McIntyre (1976, 1978). For flows in channels the transformed Eulerian-mean (TEM) approach (see e.g. Plumb & Ferrari 2005) provides a good approximation to the residual circulation (Wolfe 2013) and we adopt this approach here.

The current work consists of direct numerical simulations (DNSs) of RHC using the model defined in § 2. We seek to answer the following main questions.

- (i) How are the strength of the overturning circulation, the thermal boundary layer depth and the deep stratification affected by adding rotation to HC? Are previously proposed scaling laws consistent with the numerical simulations for different rotation rates?
- (ii) What are the effects of baroclinic instability and of the resulting baroclinic eddies in the rapidly rotating numerical simulations? How do the results compare with non-rotating HC simulations?
- (iii) How are the available potential energy  $(E_a)$  and kinetic energy  $(E_k)$  cycles modified by rotational effects? What part do the eddies play in these energy transfers?

In § 3 we review scaling arguments, show numerical solutions of non-rotating HC and discuss the criteria used to assess the accuracy of the simulations. In § 4 we discuss non-dimensional parameters and previously suggested scaling laws associated with RHC. In § 5, simulations of RHC in which baroclinic instability was suppressed (x-uniform RHC) are discussed and an analytical model capturing the essence of these solutions is described. In § 6, baroclinically active RHC solutions are presented and compared with solutions of non-rotating HC and x-uniform RHC. In § 7 we examine changes to the energy balances in the presence of rotation. Finally, in § 8 we summarize and discuss our results.

#### 2. Formulation

We consider a three-dimensional rotating fluid in a rectangular box of volume V, uniform depth H, lateral and transverse dimensions  $L_y$  and  $L_x$ , respectively. The vertical coordinate is  $-H \le z \le 0$ , and density is expressed as  $\rho = \rho_0 (1 - g^{-1}b)$ , where b is the 'buoyancy'. The Cartesian Boussinesq equations of motion are

$$\frac{\mathrm{D}\boldsymbol{u}}{\mathrm{D}t} + f\hat{\boldsymbol{k}} \times \boldsymbol{u} = -\nabla p + b\hat{\boldsymbol{k}} + \nu \nabla^2 \boldsymbol{u} - rf_b(z)(u\hat{\boldsymbol{i}} + \nu\hat{\boldsymbol{j}}), \tag{2.1a}$$

$$\frac{\mathrm{D}b}{\mathrm{D}t} = \kappa \nabla^2 b,\tag{2.1b}$$

$$\nabla \cdot \boldsymbol{u} = 0. \tag{2.1c}$$

The pressure is  $\rho_0 p$ , f is the Coriolis frequency,  $r(s^{-1})$  is the coefficient of bottom drag,  $f_b(z)$  is a near-bottom localization function defined later in (2.6) and  $\hat{k}$  is the unit vector in the vertical direction. No-penetration conditions  $\mathbf{u} \cdot \hat{\mathbf{n}} = 0$  are imposed on the top, bottom and lateral  $(\mathbf{y})$  sides, where u = (u, v, w) and  $\hat{\mathbf{n}}$  is the outward normal to the surface V. Periodic boundary conditions are prescribed in the transverse  $(\mathbf{x})$  direction to resemble the rotating tank experiments with infinite radius of curvature. The top and bottom boundary conditions are free-slip. The buoyancy flux specified at the top surface (z=0) is

$$\kappa \frac{\partial b}{\partial z} = B_{max} f(x, y) \quad \text{with } \int f(x, y) \, \mathrm{d}x \, \mathrm{d}y = 0,$$
(2.2)

where  $B_{max}$  (m<sup>2</sup> s<sup>-3</sup>) is the magnitude of the maximal buoyancy flux applied at the surface. The imposed surface flux will depend primarily on y, with variability in x introduced only as a means of perturbing the forcing. On the other five faces of V,  $\nabla b \cdot \hat{n} = 0$ . Throughout the paper  $\langle \cdot \rangle$  denotes a volume average,  $\hat{\cdot}$  denotes a spatial average over the horizontal area  $A = L_x \times L_y$ ,  $\bar{\cdot}$  denotes an average over the transverse length  $L_x$  and eddies (denoted by ') are defined as perturbations from the transverse average.

The non-dimensional parameters that govern non-rotating HC are the fixed-buoyancy Rayleigh number Ra, the fixed-flux Rayleigh number Ra, the Prandtl number Pr and the aspect ratio  $\alpha$  (Hughes & Griffiths 2008) defined as

$$Ra \equiv \frac{b_{max}L_y^3}{v\kappa}, \quad Ra_B \equiv \frac{B_{max}L_y^4}{v\kappa^2}, \quad Pr \equiv \frac{v}{\kappa}, \quad \alpha \equiv \frac{H}{L_y}.$$
 (2.3)

Here  $b_{max}$  (ms<sup>-2</sup>) is the maximal specific buoyancy at the top and  $B_{max}$  is described in (2.2). Typically in HC, the nature of the buoyancy boundary condition determines which of the Rayleigh numbers is known *ab initio* and which is part of the solution.

The two numbers are related via the Nusselt number  $Nu \equiv Ra_B/Ra$  (Hughes & Griffiths 2008), which measures the ratio between convective to conductive buoyancy transport along the lateral length of the box  $L_v$ .

The volume-averaged, kinetic  $(E_k)$ , potential  $(E_p)$ , background potential  $(E_b)$  and available potential  $(E_a \equiv E_p - E_b)$  energy equations for this model take the form (Winters & Young 2009)

$$\frac{\mathrm{d}\langle E_k \rangle}{\mathrm{d}t} \equiv \frac{1}{V} \frac{\mathrm{d}}{\mathrm{d}t} \left( \frac{1}{2} \int |\boldsymbol{u}|^2 \, \mathrm{d}V \right) = \langle wb \rangle - \nu \langle \|\boldsymbol{\nabla}\boldsymbol{u}\|^2 \rangle - r \langle f_b(z) \, |\boldsymbol{u}_H|^2 \rangle, \tag{2.4a}$$

$$\frac{\mathrm{d}\langle E_p \rangle}{\mathrm{d}t} \equiv \frac{1}{V} \frac{\mathrm{d}}{\mathrm{d}t} \left( \int -zb \, \mathrm{d}V \right) = -\langle wb \rangle + \frac{\kappa}{H} \Delta \widehat{b}, \tag{2.4b}$$

$$\frac{\mathrm{d}\langle E_b \rangle}{\mathrm{d}t} \equiv \frac{1}{V} \frac{\mathrm{d}}{\mathrm{d}t} \left( \int -z_* b \, \mathrm{d}V \right) = \kappa \left\langle \frac{\mathrm{d}z_*}{\mathrm{d}b} \left| \nabla b \right|^2 \right\rangle - \frac{\kappa}{H} z_* (\widehat{b_{top}}) \widehat{b_z}(0), \tag{2.4c}$$

$$\frac{\mathrm{d}\langle E_a \rangle}{\mathrm{d}t} \equiv \frac{1}{V} \frac{\mathrm{d}}{\mathrm{d}t} \left( \int (z_* - z) b \, \mathrm{d}V \right) 
= -\langle wb \rangle - \kappa \left\langle \frac{\mathrm{d}z_*}{\mathrm{d}b} \left| \nabla b \right|^2 \right\rangle + \frac{\kappa}{H} \Delta \widehat{b} + \frac{\kappa}{H} z_* (\widehat{b_{top}}) \widehat{b_z}(0), \tag{2.4d}$$

where  $z_*(b, t)$  is the reference height in the minimum potential energy state of a fluid with buoyancy b(x, t) (Winters *et al.* 1995),  $u_H = (u, v)$  and  $\Delta \hat{b} = \hat{b}(0) - \hat{b}(-H)$ .

The model equations (2.1) are solved using the three-dimensional spectral model **flow\_solve** (Winters & de la Fuente 2012). The fixed-flux boundary condition (2.2) is implemented using a forcing term  $\mathcal{F}(y, z)$  in (2.1b) of the form

$$\frac{\mathrm{D}b}{\mathrm{D}t} - \kappa \nabla^2 b = \mathcal{F}(y, z) \equiv S e^{-(z/\sigma_z)^2} (e^{-(y/\sigma_y)^2} - e^{-([y-L_y]/\sigma_y)^2}), \tag{2.5}$$

where  $\sigma_z = O(\Delta z)$  and  $\Delta z$  is the grid spacing in the  $\hat{k}$  direction. In the limit of infinite resolution  $(\Delta z \to 0)$  the inhomogeneity in the boundary condition is exactly exchanged for inhomogeneity in the governing equation (Winters & de la Fuente 2012) so that (2.5) and (2.2) are identical. The length  $\sigma_y$  is chosen to confine the negative/positive buoyancy source/sink to the upper corners of the domain. The corresponding maximal surface buoyancy flux  $B_{max} = (g/\rho_0)\sqrt{\pi}S\sigma_z$ . Note that  $\int \mathcal{F}(y,z) \, \mathrm{d}y = 0$  to ensure mass conservation.

The form of the bottom drag  $f_b(z)$  in (2.1a) is

$$f_b(z) = e^{-([z+H]/\sigma_d)^2},$$
 (2.6)

where  $\sigma_d = 6 \Delta z$ , which smoothly confines the action of the drag term to a thin but well-resolved near-bottom layer. Bottom drag was only used for the baroclinically active RHC simulations (see § 6).

For the baroclinically active RHC simulations, the forcing term  $\mathscr{F}$  in (2.5) was perturbed as follows:

$$\frac{\mathrm{D}b}{\mathrm{D}t} - \kappa \nabla^2 b = \mathscr{F}(y, z) \left( 1 + dS \left( e^{-(x - [L_x/2 + \sigma_x]/\sigma_x)^2} - e^{-(x - [L_x/2 - \sigma_x]/\sigma_x)^2} \right) \right), \quad (2.7)$$

in order to trigger baroclinic instability. Here  $dS = 0.005 \times S$  and  $\sigma_x$  was set to six times the grid spacing in the  $\hat{i}$  direction ( $\hat{i}$  being the unit normal in the transverse direction). This introduces a total perturbation of 1%, sufficient to initiate baroclinic instability while exactly maintaining the mass flux of the unperturbed runs.

Simulation number	$Ra_B$	Q	$nz \times ny \times nx$	Comments
1	$3.8 \times 10^{9}$	0	$65 \times 257 \times 50$	Non-rotating HC
2	$6.3 \times 10^{10}$	0	$257 \times 801 \times 1$	Non-rotating HC
3	$1.1 \times 10^{8}$	0-2	$129 \times 257 \times 1$	x-uniform RHC, varying $Q$
4	$6.0 \times 10^{8}$	0-2	$193 \times 401 \times 1$	x-uniform RHC, varying $Q$
5	$1.7 \times 10^{9}$	0-2	$257 \times 513 \times 1$	x-uniform RHC, varying $Q$
6	$1.0 \times 10^{10}$	0-2	$289 \times 801 \times 1$	x-uniform RHC, varying $Q$
7	$5.4 \times 10^{10}$	0-2	$385 \times 1201 \times 1$	x-uniform RHC, varying $Q$
8	$6.3 \times 10^{10}$	1	$257 \times 801 \times 1$	x-uniform RHC
9	$3.8 \times 10^{9}$	10	$65 \times 257 \times 1$	x-uniform RHC
10	$6.3 \times 10^{10}$	15	$257 \times 801 \times 1$	x-uniform RHC
11	$1.3 \times 10^{12}$	24	$257 \times 1025 \times 1$	x-uniform RHC
12	$3.8 \times 10^{9}$	10	$65 \times 257 \times 150$	Baroclinically active RHC, free slip
13	$3.8 \times 10^{9}$	10	$65 \times 257 \times 150$	Baroclinically active RHC, bottom drag
14	$6.0 \times 10^{10}$	15	$65 \times 513 \times 300$	$\alpha = 1/8$ , $Ro_T = 0.04$ , bottom drag
15	$2.0 \times 10^{11}$	6	$65 \times 513 \times 300$	$\alpha = 1/8$ , $Ro_T = 0.24$ , bottom drag
16	$2.0 \times 10^{11}$	0	$65 \times 801 \times 1$	$\alpha = 1/8, Ro_T \rightarrow \infty$

TABLE 1. Values of  $L_y = 1.25 \times L_x$ ,  $\alpha = 1/4$  (except for simulations 14–16), Pr = 7, Q is defined in (4.2). All simulations were integrated for at least half of a diffusive time  $(H^2/\kappa)$ .

The relatively small value of  $\sigma_x$  perturbs a wide range of transverse wavenumbers and thus allows the evolving flow to select the most unstable wavenumber. The perturbation to the forcing (2.7) was only applied during an initiation stage of the simulations spanning the first 0.01 diffusive times  $(H^2/\kappa)$ , which was at most  $\sim 1\%$  of an entire simulation time.

The numerical simulations presented in this paper model thermally driven HC (Pr = 7). Table 1 summarizes the simulations presented in this paper.

#### 3. Non-rotating HC

Rossby (1965) suggested scaling laws that provide a satisfactory condensation of numerical simulations and laboratory experiments of non-rotating HC. Performing laboratory experiments with fixed-temperature boundary conditions, he first assumed that the typical vertical variation of buoyancy within the thermal boundary layer of thickness  $\delta_R$  is  $b_{max}$ . He further assumed that the dominant balance in the vertical momentum equation is hydrostatic, and that, in the horizontal momentum equations, the pressure force is balanced by vertical viscosity. Finally, he assumed that the balance in the buoyancy (2.1b) is between the advective terms  $u \cdot \nabla b$  and vertical diffusion  $\kappa b_{zz}$ . The resulting scaling law is

$$\delta_R \sim \frac{L_y}{Ra^{1/5}} \sim \frac{L_y}{Ra_R^{1/6}},\tag{3.1}$$

where the scaling law in terms of  $Ra_B$  is derived using  $\kappa b_{max} \delta_R^{-1} \sim B_{max}$ . The corresponding lateral velocity scale  $v_R$  and x-averaged streamfunction scale  $\psi_R$  can be found using  $v_R \sim \kappa L_y \delta_R^{-2}$ ,  $\psi_R \sim \kappa L_y \delta_R^{-1}$ . Two things should be kept in mind regarding Rossby's scaling law (3.1). First, it is thought to hold in the interior of the flow away from the lateral side boundaries. Second,  $\delta_R$  is independent of the domain depth H, implying that  $\delta_R/H \ll 1$ . Chiu-Webster et al. (2008) discuss the nature of the

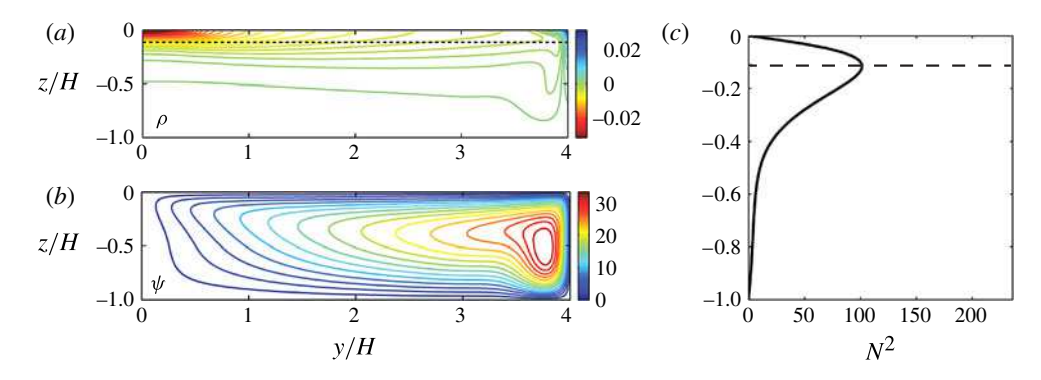


FIGURE 1. (a) Steady-state, x-averaged density normalized by  $HB_{max}\rho_0/g\kappa$ , (b) streamfunction normalized by  $\kappa$  and (c) horizontally averaged interior stratification normalized by  $(B_{max}/L_y^2)^{2/3}$ , for simulation 1. Dashed lines represent the thermal boundary layer depth according to Rossby's scaling law (3.1).

flow when  $\delta_R/H \sim O(1)$ . In this regime the analytical solution proposed by Smith (1976) to describe estuarine dynamics, can be modified to describe HC dynamics quite accurately.

Estimating Rossby's scaling laws using molecular oceanographic values corresponding to a temperature difference of 25 K, a thermal expansion coefficient of  $2 \times 10^{-4}$  K<sup>-1</sup>,  $L_y = 10 \times L_x = 2000 \times H = 10^7$  m and  $\nu = 10 \times \kappa = 10^{-7}$  m² s<sup>-1</sup> yields  $\delta_R = 2.9$  m,  $\nu_R = 0.12$  ms<sup>-1</sup> and  $\psi_R = 0.35$  Sv. If turbulent values are used ( $\nu = \kappa = 10^{-5}$  m² s<sup>-1</sup>), then  $\delta_R = 11.5$  m,  $\nu_R = 0.75$  ms<sup>-1</sup> and  $\psi_R = 8$  Sv.

Figure 1(a) shows a typical, steady-state, x-averaged, density field of non-rotating HC. Qualitatively, the flow develops a box-scale lateral density gradient within a boundary layer that forms near the top (z=0). This lateral density gradient drives a flow towards the destabilizing (cold) end, where a plume is formed that penetrates to full depth. The volume transport in the plume is returned laterally along the bottom boundary (z=-H). The circulation is closed via slow vertical flow in the interior of the domain. Away from the lateral boundaries the vertical density structure is everywhere very similar to the horizontally averaged stratification shown in figure 1(c), with a clear maximum at  $z \sim -\delta_R$  (dashed line) and an unstratified abyss. In oceanography, such a clear maximum is often used to define the thermocline. The x-averaged streamfunction shows a single, clockwise overturning cell extending almost throughout the entire lateral domain as can be seen in figure 1(b). Figure 2 shows that advection is the dominant mechanism for the lateral buoyancy flux in this flow.

All of the non-rotating and the x-uniform rotating simulations (§ 5) presented in this paper reached a complete, pointwise steady state and there was no difference between three-dimensional and two-dimensional simulations of these kinds. The perturbation to the forcing term  $\mathscr{F}$  of the form (2.7) made no difference when applied to the non-rotating HC simulations and triggered baroclinic instability when applied to RHC simulations (§ 6). In order to verify that all simulated fields were resolved down to the viscous scale, the spectra of the second derivative (highest derivative in these simulations) of density in each direction were analysed. The value of Pr was 7 for all simulations, so density fields exhibit the smallest scale in these simulations and the second derivative of density is the hardest computed field to resolve. The decay in the spectra of the second derivative down to the highest wavenumber was

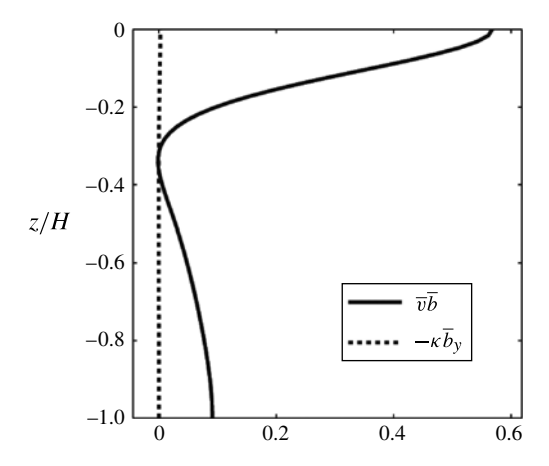


FIGURE 2. Lateral, *x*-averaged, advective (solid) and diffusive (dash) buoyancy flux at  $y = L_y/2$ , for the simulation in figure 1. Fluxes are normalized by  $B_{max}$ .

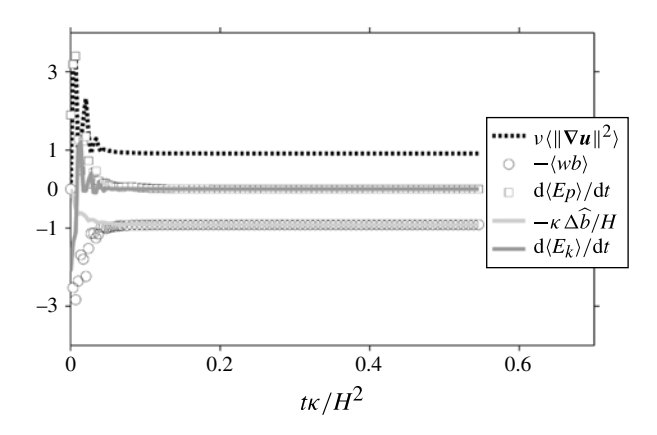


FIGURE 3. Time series of the different terms in (2.4a), (2.4b) normalized by  $|\langle wb \rangle|$ , for simulation 2.

the first criterion used to ensure sufficient resolution. Second, because the laterally integrated forcing at the top boundary (2.5) is zero by construction, the change in total mass should remain zero at all times. Therefore the change in mass, normalized by  $(\rho_0/g)S\sigma_z\sqrt{\pi}L_y^2L_xL_z\kappa^{-1}$ , was computed as a function of time to measure solution quality. The normalized change in mass was less than  $1\times 10^{-14}$  in all simulations. Finally, conservation of equations (2.4a) and (2.4b) normalized by  $|\langle wb\rangle|$  to within  $\sim 1\times 10^{-4}$ , was the last criterion used to ensure sufficient resolution and agreement with the simulated equations of motion. Figure 3 shows a plot of the different terms in (2.4a) and (2.4b) for a typical simulation of non-rotating HC (simulation 2). The fact that  $d\langle E_k\rangle/dt=d\langle E_p\rangle/dt=0$  along with  $\nu\langle ||\nabla u||^2\rangle=\kappa\,\Delta \hat{b}/H=\langle wb\rangle$  indicates that the flow has reached a completely steady state.

#### 4. Adding rotation

The scaling law (3.1) has been verified by multiple authors (see § 1 for references), which motivates non-dimensionalizing (2.1) with  $f \neq 0$  using  $\delta_R$ ,  $v_R$ , as proposed previously by Hignett *et al.* (1981). This leads to the non-dimensional momentum equations:

$$\frac{1}{Pr}\frac{\mathbf{D}\boldsymbol{u}}{\mathbf{D}t} + Q\hat{\boldsymbol{k}} \times \boldsymbol{u} = -\frac{1}{\alpha}\nabla_{H}p + Ra^{2/5}\left(-\frac{\partial p}{\partial z} + b\right)\hat{\boldsymbol{k}} + \nabla^{2}\boldsymbol{u},\tag{4.1}$$

where, for simplicity,  $L_y = L_x = L$ ,  $\nabla^2 = \alpha^2 (\partial^2/\partial y^2 + \partial^2/\partial x^2) + \partial^2/\partial z^2$  and  $\nabla_H = \alpha(\partial/\partial x, \partial/\partial y)$ . The non-dimensional number

$$Q = 2\left(\delta_R/d\right)^2 \tag{4.2}$$

describes the rotation rate in rotating convection systems (King *et al.* 2009),  $\delta_R$  is defined in (3.1) and  $d = \sqrt{2\nu/f}$  is the Ekman depth. Killworth & Manins (1980) show that  $Pr \ge 5$  is sufficiently large for the material derivative in (4.1) to be ignored. For Q = 0 (no rotation) we thus recover the momentum balance leading to (3.1).

We now provide a short review of scaling laws previously suggested for the thermal boundary layer depth in RHC. These are linear scaling laws, in the sense that they ignore the effects of baroclinic eddies. In all cases the velocity and streamfunction scales can be determined using  $v \sim \kappa L_y \delta^{-2}$  and  $\psi \sim \kappa L_y \delta^{-1}$ . We find it illuminating to present these results as modifications to the non-rotating scales (Rossby scales).

Robinson & Stommel (1959) proposed the same dominant balance in the vertical momentum equation and buoyancy equation as Rossby. However, in the horizontal momentum equation the rotation term is assumed to balance the pressure term (geostrophic balance). These assumptions lead to the following thermal boundary layer scale (subscript RS):

$$\delta_{RS} \sim Q^{1/3} \delta_R \sim Q^{1/4} \delta_{R_R},\tag{4.3}$$

where the subscript B denotes fixed flux scales for  $\delta_R$  in (3.1). Stern (1975) assumed the same momentum balance as RS. However, instead of incorporating the buoyancy equation, he proposed a balance in the  $E_k$  equation (2.4a) between the buoyancy flux term  $\langle wb \rangle$  and the  $E_k$  dissipation  $v \langle || \nabla u ||^2 \rangle$ . His main assumption was that  $\langle wb \rangle$  is dominant throughout the entire thermal boundary layer whereas dissipation occurs mainly in the Ekman layer. This new balance leads to the following thermal boundary layer scale (subscript St):

$$\delta_{St} \sim Q^{3/4} \delta_R \sim Q^{1/2} \delta_{R_R}. \tag{4.4}$$

Note that for  $Q \sim O(1)$  there is a three-term balance between the rotation, pressure and viscous terms in the horizontal components of (4.1), and based on (4.3), (4.4) the thermal boundary layer should still scale like  $\delta_R$ .

Using oceanic, basin scale values on an f-plane ( $L_y = 10^6$  m,  $f = 10^{-4}$  s<sup>-1</sup>) yields Q = 130 and 210 for molecular and turbulent values, respectively (using parameters defined in § 3). The ocean is therefore rapidly rotating and it is of interest to examine solutions in the regime  $Q \gg 1$ . In all of the above scaling laws the f-plane approximation leads to constant Q. In the ocean the latitudinal variation in Coriolis force is clearly important. The correction to the above scaling can be incorporated simply by considering Q = Q(y).

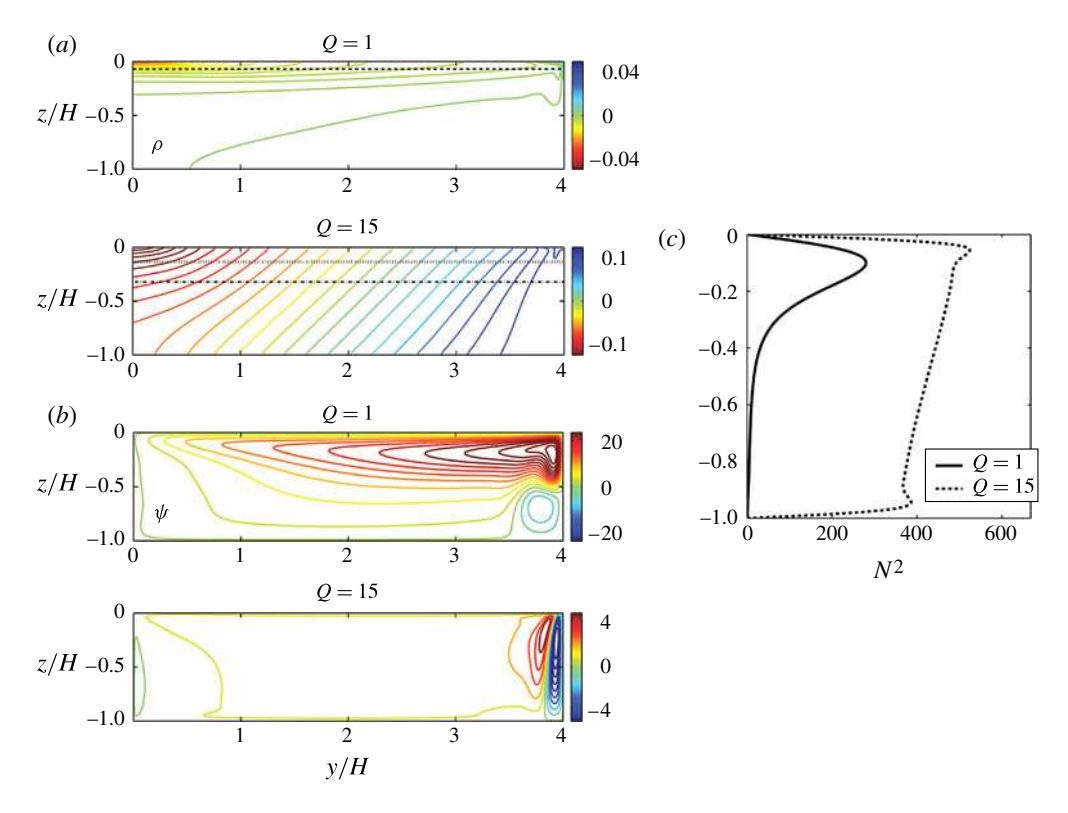


FIGURE 4. (a) Steady-state x-averaged density normalized by  $HB_{max}\rho_0/g\kappa$ , (b) streamfunction normalized by  $\kappa$  and (c) horizontally averaged, interior stratification normalized by  $(B_{max}/L_y^2)^{2/3}$ , for x-uniform RHC. Dashed line (a, top) represents Rossby's scaling law (3.1) for the Q=1 solution (simulation 8). Vertically dashed and dot-dashed lines (a, bottom) represent Robinson & Stommel's scaling law (4.3) and Stern's scaling law (4.4), respectively, for the Q=15 solution (simulation 10).

#### 5. x-Uniform RHC

In order to illustrate the effects of rotation, while suppressing baroclinic instability, we first examine unperturbed RHC solutions which are uniform in  $\hat{i}$ . In these solutions, rapid rotation is expected to halt the lateral, return volume transport from the plume region at a distance of a Rossby radius of deformation  $(R_d)$  from the cold end  $(y = L_y)$ . If the rotation rate is not too high, i.e.  $Q \sim O(1)$ , then  $R_d \gg L_y$ , and we expect little change from the non-rotating solution.

Figure 4(a) shows typical, steady-state, x-uniform density fields of RHC. For Q=1 the solution is similar to the non-rotating solution, in agreement with the laboratory results of Hignett  $et\ al.\ (1981)$  and Park & Whitehead (1999). For Q=15, however, the solution is substantially different with no apparent thermal boundary layer (or thermocline). In the interior, away from the lateral sides  $(y=0,L_y)$  there is an extensive region in which the isopycnals touch both top and bottom boundaries. The corresponding, horizontally averaged stratification (figure 4c) shows that for Q=15 there is an increase in stratification throughout the domain with two local maxima, presumably near the top and bottom Ekman layers. The streamfunction (figure 4b) shows a substantial decrease in magnitude from the Q=1 to the Q=15 case, with

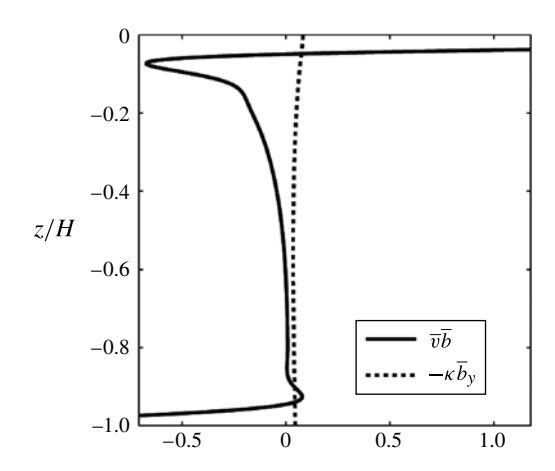


FIGURE 5. Lateral, *x*-averaged, advective (solid) and diffusive (dashed) buoyancy flux at  $y = L_y/2$ , for simulation 10 (Q = 15). Fluxes are normalized by  $B_{max}$ .

an anti-clockwise circulation pattern next to the plume region. This structure develops because the heavy fluid in the cold end, which flows in the positive  $\hat{i}$  direction as it falls, is deflected away from the sidewall by the Coriolis force. Continuity then produces a compensating updraft adjacent to the sidewall producing the two-cell circulation pattern. This feature is enhanced with increasing rotation. Figure 5 shows that, unlike the non-rotating case (figure 2), diffusion is the dominant mechanism for lateral buoyancy flux in the rapidly rotating simulations outside the thin top and bottom Ekman layers.

In non-rotating HC the Nusselt number and Péclet number  $Pe = \psi_{max}/\kappa$  should scale like  $Ra^{1/5}$  (Chiu-Webster et al. 2008). Figure 6 shows Nu and Pe versus  $Ra^{1/5}$  for a set of x-uniform RHC simulations in which Q varies between 0 at y=0 and 2 at  $y=L_y$ . The good agreement between the numerical simulations and Rossby's scaling law confirm its applicability for  $Q \sim O(1)$  simulations, even for varying Q (corresponding to laterally varying f). Note that both RS (4.3) and St (4.4) scaling laws reduce to Rossby's scaling law in this regime. Similar analyses for a set of Q > 1 simulations (not shown) demonstrated no such agreement between any of the previously suggested scaling laws (4.3), (4.4) and the x-uniform RHC simulations.

#### 5.1. Analytical model

The x-uniform solutions shown in figure 4 motivate us to suggest the following analytical model in the interior region, away from the lateral boundaries where the buoyancy forcing is applied. This model is partly based on Whitehead's (1981) model for shelf circulation and is essentially an extension of Smith's (1976) solution for buoyancy-driven estuarine circulation.

Scaling the horizontal velocities using  $u, v \sim b_{max}\alpha/f$  (assuming  $L_x \sim L_y$ ), the pressure hydrostatically  $(p \sim b_{max}H)$  and assuming  $Pr \gg 1$ ,  $\alpha^2 \ll 1$ ,  $Q \sim O(1)$  and  $Ra\alpha^5 \sim O(1)$ , the dominant balance in (2.1) is

$$-f\,\tilde{v} = \nu \tilde{u}_{zz},\tag{5.1a}$$

$$f\,\tilde{u} = -\frac{\partial p}{\partial y} + \nu \tilde{v}_{zz},\tag{5.1b}$$

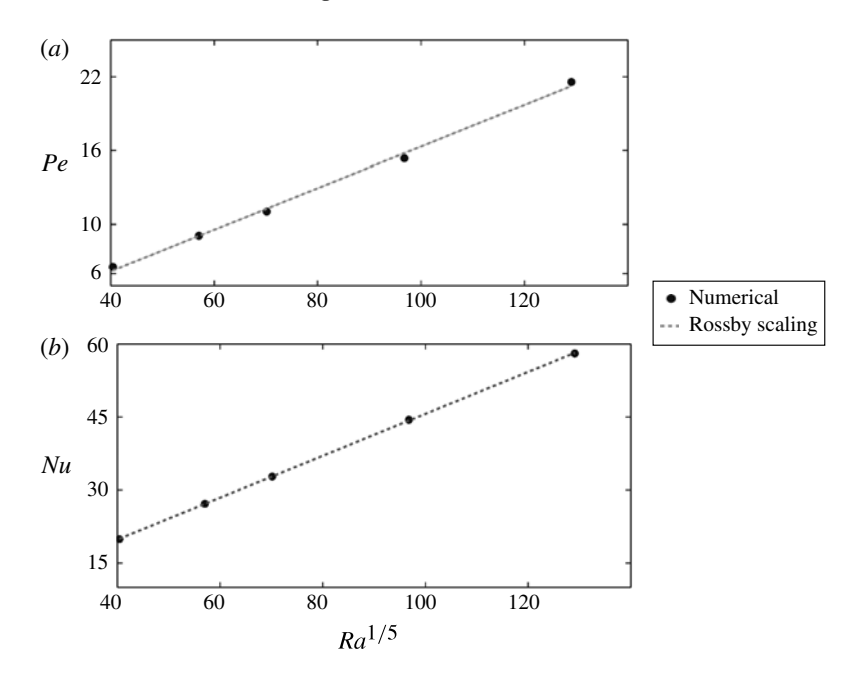


FIGURE 6. (a) Péclet number and (b) Nusselt number versus  $Ra^{1/5}$ . Here Q varies between zero in the buoyancy stabilizing (hot) end and two in the buoyancy destabilizing (cold) end (simulations 3–7).

$$0 = -\frac{\partial p}{\partial z} + b,\tag{5.1c}$$

$$-\Gamma \tilde{v} = \kappa \tilde{b}_{zz},\tag{5.1d}$$

$$\int_{-H}^{0} \tilde{v} \, \mathrm{d}z = 0 \tag{5.1e}$$

where we have also assumed the ansatz

$$b = -\Gamma y + \tilde{b}(z), \quad p = y(-\Gamma z + p_y^0) + \tilde{p}(z), \quad \mathbf{u} = (\tilde{u}(z), \tilde{v}(z), 0).$$
 (5.2)

Equation (5.1e) comes from the incompressibility condition. In (5.2),  $\Gamma$  is the (assumed) constant, lateral buoyancy gradient and  $p_y^0$  is a constant representing the lateral pressure gradient at z=0. We assume that the buoyancy flux is confined to the corner regions away form the interior (where the solution is thought to apply) and we therefore suppose  $\nabla b \cdot \hat{n} = 0$  at the top and bottom. Free slip is always assumed at the top boundary, and at the bottom boundary we apply either free slip (in accordance with the numerical simulations) or no slip. In either case inserting (5.1a) into (5.1d) leads to

$$\frac{\Gamma v}{f} \tilde{u}_{zz} = \kappa \tilde{b}_{zz}. \tag{5.3}$$

The boundary condition at the top is free slip and both the bottom and top walls are taken to be insulating, so  $\partial u/\partial z = 0$  at the bottom, irrespective of the bottom velocity boundary condition. Because  $\tilde{u}_x = 0$  it is useful to define a streamfunction such that

$$\tilde{v} = -\tilde{\psi}_z$$
 and  $\tilde{w} = \tilde{\psi}_v$ . (5.4)

Inserting (5.4) into (5.1a), integrating once making use of (5.3), and substituting into  $\partial/\partial z$  of (5.1b) we get

$$\tilde{\psi}_{4z} + \frac{4}{d^4}\tilde{\psi} = \frac{2\Gamma}{fd^2} \tag{5.5}$$

where the d is the Ekman depth defined in § 4. For free-slip top and bottom boundary conditions, the symmetry in both  $\tilde{u}$ ,  $\tilde{v}$  motivates the introduction of a new coordinate z'=z+H/2, since then  $p_y^0=0$ , simplifying the algebra. The solution to (5.5) in the new coordinate z' is

$$\tilde{u}(z') = \Gamma\left(\frac{z'}{f} + F_2(z')G_1 - F_1(z')G_2\right),$$
(5.6a)

$$\tilde{v}(z') = \Gamma(F_1(z')G_1 + F_2(z')G_2), \tag{5.6b}$$

$$\tilde{b}(z') = \frac{\Gamma \nu}{\kappa f} \tilde{u}(z'), \tag{5.6c}$$

where  $F_{1,2}(z')$  and  $G_{1,2}$  are given explicitly in (A 10).

The solution (5.6c) is correct up to a constant which vanishes in the limit  $\alpha \to 0$ . The solution for no-slip boundary condition at the bottom is described in (A 1)–(A 8).

In order to determine  $\Gamma$  for either of the bottom velocity boundary conditions one must apply conservation of flux in the form

$$|\mathscr{F}_{1/2}| = \int (\tilde{v}\tilde{b} + \kappa \Gamma) \,\mathrm{d}z,\tag{5.7}$$

where  $|\mathscr{F}_{1/2}| = (\pi g/4\rho_0)S\sigma_z\sigma_y = (\sqrt{\pi}/4)\sigma_yB_{max}$  is the magnitude of the buoyancy source/sink determined from the numerical boundary condition defined in (2.5). Calculating the integral in (5.7) leads to

$$\Gamma^3 \mathcal{H}_{fx} + \Gamma \kappa H = |\mathcal{F}_{1/2}| \tag{5.8}$$

where  $\mathcal{H}_{fs}$  is a positive constant written explicitly in (A11). Finding  $\Gamma$  therefore reduces to finding the single real root of the cubic (5.8).

The analytical model described above is valid when the ratio between the lateral extent of a typical sloping isopycnal  $\Delta_y$  and the lateral extent of the domain  $L_y$  is small, so we write

$$\beta \equiv \frac{\Delta_y}{L_y} = \frac{\tilde{b}_{top} - \tilde{b}_{bot}}{\Gamma L_y} \ll 1 \tag{5.9}$$

as the condition of validity.

#### 5.1.1. Rapidly rotating analytical solution

It is illuminating to examine the analytical solution in the rapidly rotating limit  $Q\gg 1$  which is most relevant to the oceanic regime. This limit corresponds to the regime  $Ra\alpha^5\gg 1$  using the scales leading to (5.1) with the lateral velocity  $v\sim v/(fH^2)u$  (in this regime  $v\ll u$ ), which makes the viscous term in (5.1b) negligible. This can be done by taking the limit  $d\to 0$  of (5.6) in the free-slip case and of (A 1)–(A 8) in the no-slip case, leading to

$$\tilde{u}_I = \frac{\Gamma z - p_y^0}{f},\tag{5.10}$$

where the subscript I indicates that the rapidly rotating solution is in the interior, between the thin, top and bottom Ekman layers. For free-slip bottom boundary condition, using the same transformation as before (z'=z+H/2) leads to  $p_y^0=0$  and z should be replaced by z' in what follows. For no-slip bottom boundary condition,  $p_y^0=-\Gamma H$  (assuming the bottom Ekman layer is thin so that the boundary condition is applied at z=-H). The remaining fields are

$$\tilde{\psi}_I = v \frac{\Gamma}{f^2}, \quad \tilde{v}_I = 0, \quad b_I \approx -\Gamma y + z Pr \left(\frac{\Gamma}{f}\right)^2.$$
 (5.11)

Then (5.8) becomes

$$\Gamma\left(\frac{Pr^2}{f^4}\Gamma^2 + 1\right) = \frac{|\mathscr{F}_{1/2}|}{\kappa H},\tag{5.12}$$

and the validity condition (5.9) is now

$$\beta = Pr\alpha \frac{\Gamma}{f^2} \ll 1. \tag{5.13}$$

This condition is satisfied in both the ocean (using parameters defined in § 3) and in the numerical simulations.

If we scale  $\Gamma$  using  $b_{max}/L_v$ , equation (5.12) can be written as

$$\left(Pr^2Ro_T^2 + 1\right) = \frac{|\mathscr{F}_{1/2}|}{\kappa\alpha b_{max}},\tag{5.14}$$

suggesting that the size of the lateral buoyancy gradient depends on  $Pr^2Ro_T^2$ , where

$$Ro_T \equiv \frac{b_{max}}{f^2 L_{v}},\tag{5.15}$$

is the thermal Rossby number measuring the ratio between the length scale on which rotation is affecting buoyancy  $(b_{max}/f^2)$  to the domain length  $(L_y)$ . In the oceanic regime  $Ro_T \sim O(1)$  and  $Pr^2Ro_T^2 \gg 1$ . The corresponding lateral buoyancy gradient  $\Gamma$  in this regime is

$$\Gamma = \left(\frac{f^4|\mathscr{F}_{1/2}|}{\kappa P r^2 H}\right)^{1/3}.$$
 (5.16)

Figure 7 shows a comparison between a steady-state, x-uniform, interior buoyancy field, computed from a numerical simulation (a) and from the rapidly rotating analytical solution (5.11) (b). Good qualitative agreement is seen in the isopycnal slopes, although there is a difference in absolute values. This difference is expected to vanish in the limit  $\alpha \to 0$ . The horizontally averaged, interior stratification (c) and streamfunction (d) are shown along with the predicted analytical values in dashed lines. The maximal difference between theory and simulation in both cases is  $\sim 10 \%$  in the bottom of the top Ekman layer. The numerically computed lateral buoyancy gradient normalized by  $B_{max}/\kappa$  at z/H = -1/2 is  $\Delta b/\Delta y = 0.054$ . The normalized analytical prediction (5.8) gives  $\Gamma = 0.055$ . Similar accuracies were obtained for all other x-uniform RHC simulations.

#### 5.1.2. Stability analysis

The sloping isopycnals of the rapidly rotating x-uniform solutions produce greatly enhanced available potential energy and, consequently, one expects the flow to be

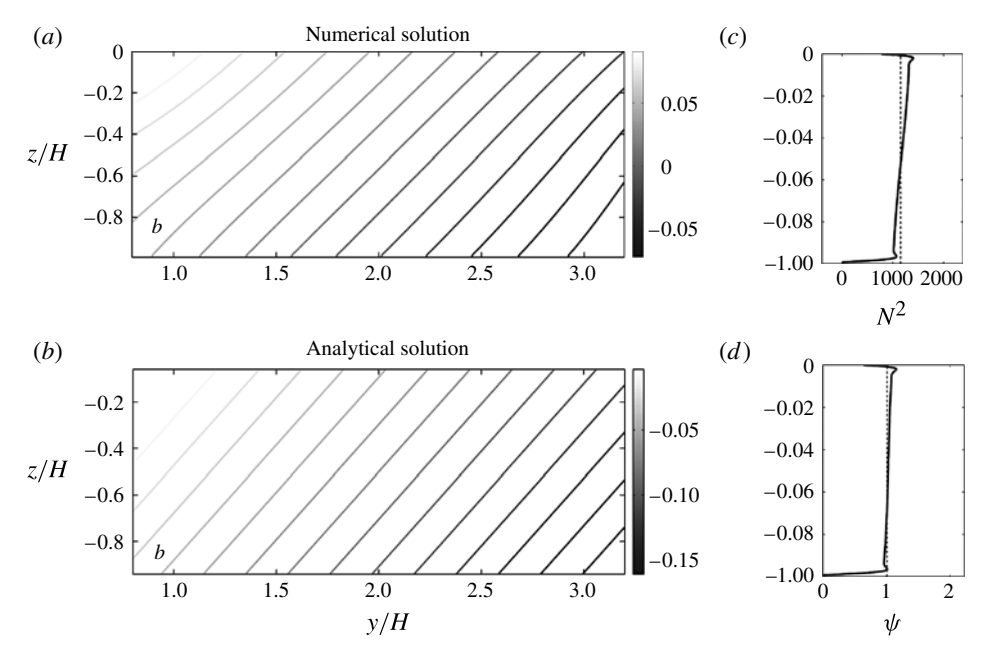


FIGURE 7. (a) Interior, x-averaged, steady-state buoyancy normalized by  $HB_{max}/\kappa$  for x-uniform RHC simulation and (b) the corresponding analytical field (5.11). (c) Horizontally averaged interior stratification normalized by  $(B_{max}/L_y^2)^{2/3}$  and (d) streamfunction normalized by  $\kappa$ , for the numerical solution in (a). Dashed lines in (c,d) represent the predicted analytical values  $\partial \tilde{b}_I/\partial z$  and  $\tilde{\psi}_I$  in (5.11), respectively. Numerical fields are computed from simulation 11 (Q=24).

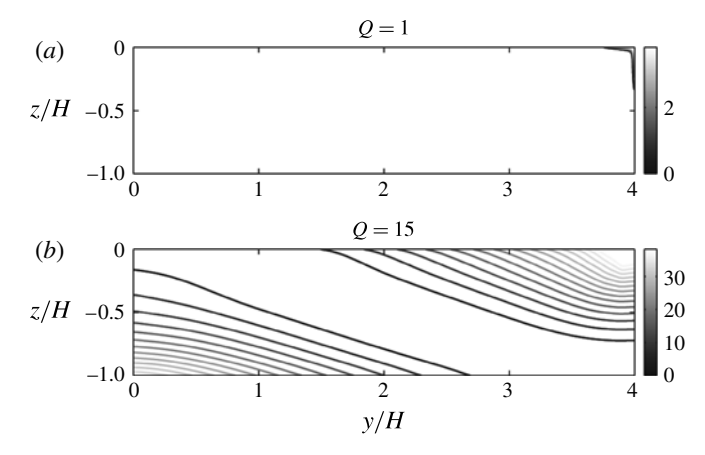


FIGURE 8. Available potential energy density  $\mathcal{E}_a$  normalized by  $(B_{max}L_y)^{2/3}$ , for (a) non-rotating HC and (b) x-uniform RHC, from simulations 2 and 10.

baroclinically unstable. Figure 8 shows a comparison of the available potential energy density,  $\mathcal{E}_a$ , for non-rotating HC (a) and for x-uniform RHC (b). Here  $\mathcal{E}_a$  is the positive-definite spatial contribution of available potential energy, which integrates to  $E_a$  (2.4d) (Andrews 1981; Holliday & McIntyre 1981; Scotti, Beardsley & Butman 2006; Roullet & Klein 2009; Molemaker & McWilliams 2010; Winters & Barkan 2012).

The tendency of the *x*-uniform flow to become unstable can be analysed by performing linear stability analysis on the rapidly rotating analytical solution (5.10)–(5.11). The non-dimensional parameter that indicates the type of instability with the largest growth rate is the Richardson number (Stone 1966). In the rapidly rotating solution  $Ri \equiv \tilde{b}_{I_z}/\tilde{u}_{I_z} = Pr > 1$ . This suggests that the quasigeostrophic (QG) modes have the largest growth rate (Stone 1966), although other modes of instability are also present. Nevertheless, if the Ekman layers are ignored the rapidly rotating solution (§ 5.1) is the basic state of the Eady problem (Eady 1949) and the QG approximation does a good job in predicting the largest wavelength of instability (Cessi & Fantini 2004). The resulting QG predictions for the critical and maximal wavelengths of instability are  $\lambda_c = 2.62R_d$  and  $\lambda_m = 3.9R_d$ , respectively, where  $R_d \equiv NH/f = \sqrt{Pr} \Gamma H/f^2$  is the Rossby radius of deformation. These predictions were used to guide us in choosing sufficiently large transverse domains ( $L_x$ ) for the baroclinically active RHC simulations (§ 6). Given resource constraints, baroclinically active RHC simulations were carried out using  $L_x \sim L_y \geqslant 10R_d$ .

Note that the critical rotation rate value ( $Q_c$ ) above which baroclinic instability is expected to develop depends on the other non-dimensional parameters that govern RHC (2.3). Hignett *et al.* (1981) have performed a linear stability analysis which accounted for the top Ekman layer as well. They found the following relation for the critical rotation rate

$$Q_c > \left(Pr\left(\frac{R_d}{L_x}\right)^2\right)^{-4/11}. (5.17)$$

Given the Pr of our simulation and the requirement  $L_x \sim L_y \ge 10R_d$ , we expect instability to occur for  $Q_c > 2.63$ .

#### 6. Baroclinically active RHC

We now turn our attention to simulations of RHC with transverse variations, which allow for baroclinic instability and the generation of baroclinic eddies that release the available potential energy stored in the sloping isopycnals. The differences between these simulations and the x-uniform simulations are the small perturbation to the forcing term (2.7).

The TEM formalism, introduced by Andrews & McIntyre (1976, 1978) provides a useful framework for discussing eddy effects under a wide range of conditions. For channel flows the TEM equations rely on the transformation from the Eulerian x-mean velocity  $\overline{u}$  to the residual mean velocity  $\overline{u}_{res}$ , following

$$\overline{u}_{res} = \overline{u} + \overline{u}^* = \overline{u} + \nabla \times \hat{i}\psi^*, \tag{6.1}$$

where  $\bar{u}^*$ ,  $\psi^*$  are the velocity, streamfunction associated with the eddies and  $\hat{i}$  is the unit vector in the transverse direction. Consider the x-average of (2.1b),

$$\frac{\partial \overline{b}}{\partial t} + \overline{\boldsymbol{u}} \cdot \nabla \overline{b} = \kappa \nabla^2 \overline{b} - \nabla \cdot \boldsymbol{F} \{b\}, \tag{6.2}$$

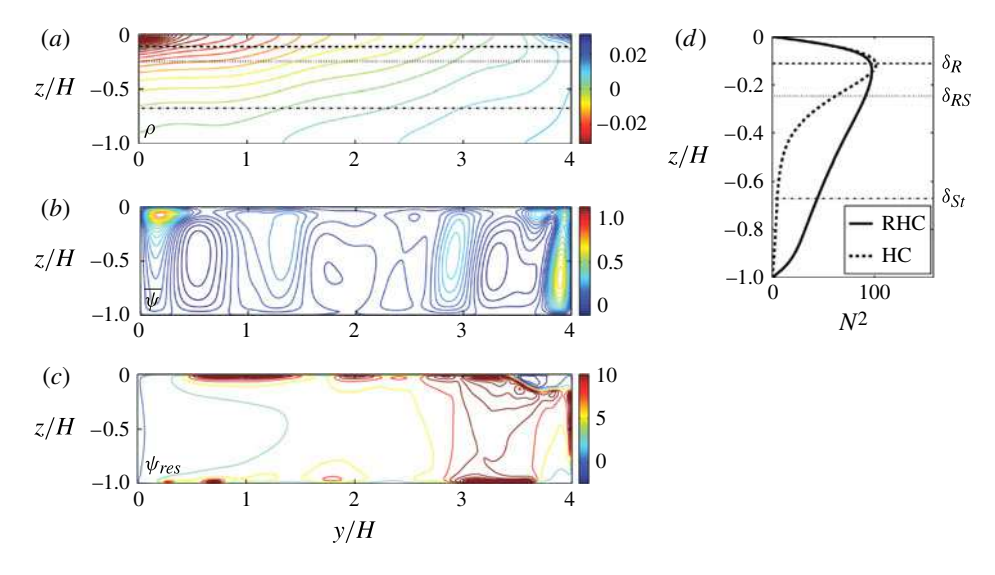


FIGURE 9. (a) Statistically steady, x-averaged density normalized by  $HB_{max}\rho_0/g\kappa$ , (b) x-averaged streamfunction normalized by  $\kappa$ , (c) the residual streamfunction  $\overline{\psi} + \psi^*$  normalized by  $\kappa$  and (d) horizontally averaged, interior stratification normalized by  $(B_{max}/L_y^2)^{2/3}$ , for baroclinically active RHC (simulation 13, Q=10). The dashed line in (d) shows the horizontally averaged stratification for non-rotating HC. Horizontally dashed, vertically dashed and dot-dashed lines in (a,d) represent the boundary layer scaling laws proposed by Rossby (3.1), Robinson and Stommel (4.3) and Stern (4.4), respectively.

where  $F\{b\} = \overline{u'b'}$  is the eddy flux of buoyancy. Under the transformation (6.1), equation (6.2) becomes

$$\frac{\partial \overline{b}}{\partial t} + \overline{\boldsymbol{u}}_{res} \cdot \nabla \overline{b} = \kappa \nabla^2 \overline{b} - \nabla \cdot \boldsymbol{F}_{res} \{b\}, \tag{6.3}$$

where  $F_{res}\{b\}$  is the 'residual eddy flux' defined as

$$\boldsymbol{F}_{res}\{b\} = \boldsymbol{F}\{b\} - \psi^* \hat{\boldsymbol{i}} \times \nabla \overline{b}. \tag{6.4}$$

Andrews & McIntyre (1976) introduced the coordinate-independent form of the eddy streamfunction

$$\psi^* = \frac{\overline{v'b'}\,\overline{b}_z - \overline{w'b'}\,\overline{b}_y}{\overline{b}_y^2 + \overline{b}_z^2},\tag{6.5}$$

which eliminates entirely the eddy flux component that is directed along  $\bar{b}$  contours (skew flux). Consequently, if the flow is completely adiabatic then the choice (6.5) identically sets  $F_{res}\{b\} = 0$ . In the limit of small isopycnal slope  $(-\bar{b}_y/\bar{b}_z \ll 0)$ , equation (6.5) reduces to the QG form

$$\psi_{QG}^* = \frac{\overline{v'b'}}{\overline{b}_z}.\tag{6.6}$$

Figure 9 shows the statistically steady, x-averaged, density (a), streamfunction (b), residual streamfunction (c) and horizontally averaged stratification (d) for a typical

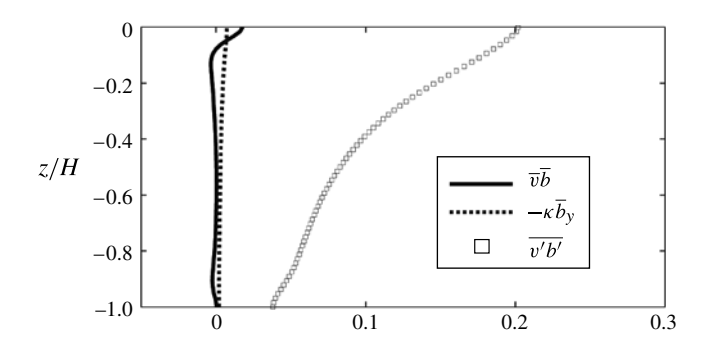


FIGURE 10. Lateral, *x*-averaged, advective (solid), diffusive (dash) and eddy (square) buoyancy flux at  $y = L_y/2$ , for simulation 13 (Q = 10). Fluxes are normalized by  $B_{max}$ .

baroclinically active RHC simulation. Time averages over the last quarter of a diffusive time  $(H^2\kappa^{-1})$  were carried out prior to computing the fields. The x-averaged density plot shows that a thermal boundary layer is again apparent. Most of the surface outcropping isopycnals no longer intersect the bottom boundary, in contrast to the x-uniform RHC simulations (figure 4). The horizontally averaged stratification in the baroclinically active RHC solution shows a maximum at a depth similar to that of non-rotating HC, and larger values of  $N^2$  at depth. Rossby's scaling law (3.1) better matches that maximum than RS scaling law (4.3) and St scaling law (4.4) (dashed, vertically dashed, and dot-dashed lines in figure 9c). The x-averaged streamfunction shows multiple overturning cells, in contrast with the single large overturning cell of the non-rotating HC simulation (figure 1). The residual streamfunction  $\psi_{res} = \overline{\psi} + \psi^*$  is an order of magnitude larger than the x-averaged streamfunction, implying that the contribution of the mean flow to the buoyancy transport is negligible in these solutions. Figure 10 further supports this point, showing that it is the eddy buoyancy flux  $\overline{v'b'}$  that dominates the lateral buoyancy flux in this flow.

Figure 11(a) shows the residual streamfunction  $\psi_{res} = \overline{\psi} + \psi^*$ , the eddy streamfunction  $\psi^*$  (b) and the QG eddy streamfunction  $\psi^*_{QG}$  (c) for a baroclinically active RHC simulation with a higher  $Ra_B$  and smaller aspect ratio than in figure 9 (simulation 15 in table 1). The overall solution is generally similar to the lower  $Ra_B$ , higher aspect ratio simulation (see § 6.2 for further discussion). As before, the residual streamfunction is dominated by the eddy component  $\psi^*$ , which, aside for thin top and bottom boundary layers, agrees well with the QG form (6.6). Note that the sense of the eddy-induced circulation is counter clockwise. This is in contrast to the x-uniform solutions where the sense of the circulation was clockwise (figure 4b, bottom). Because  $\psi_{res}$  contours do not align with density contours the eddy flux of buoyancy has a non-negligible diabatic component. Given the dominance of  $\psi^*_{QG}$  in the interior and that of  $\overline{v'b'}$  shown in figure 10, equation (5.7) becomes

$$|\mathscr{F}_{1/2}| \approx \int (\overline{v'b'}) dz \approx \int (v^*\overline{b}) dz$$
 (6.7)

(after an integration by parts and because  $\psi^*$  vanishes at the top). Equation (6.7) states that the lateral buoyancy flux in this flow is predominantly due to 'advection' by the eddy velocity  $v^*$ .

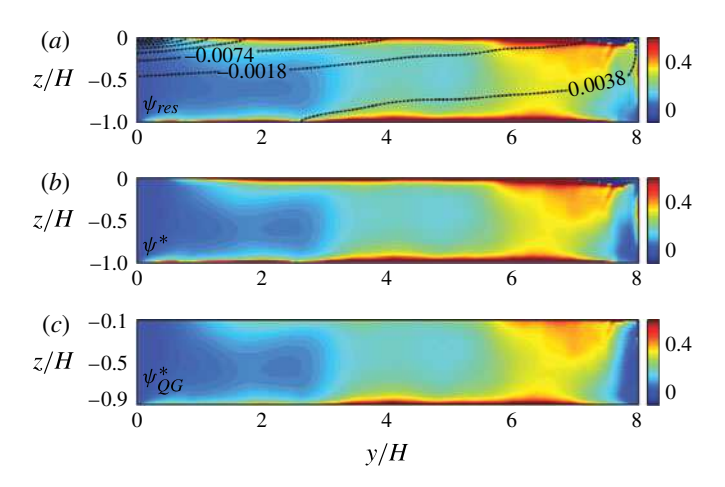


FIGURE 11. (a) The residual streamfunction  $\overline{\psi} + \psi^*$ , (b) the eddy streamfunction  $\psi^*$  (6.5) and (c) the QG streamfunction  $\psi^*_{QG}$  (6.6). Density contours in the top figure are normalized by  $HB_{max}\rho_0/g\kappa$ . Streamfunctions are normalized by  $\kappa$ . Simulation 15 (Q=6).

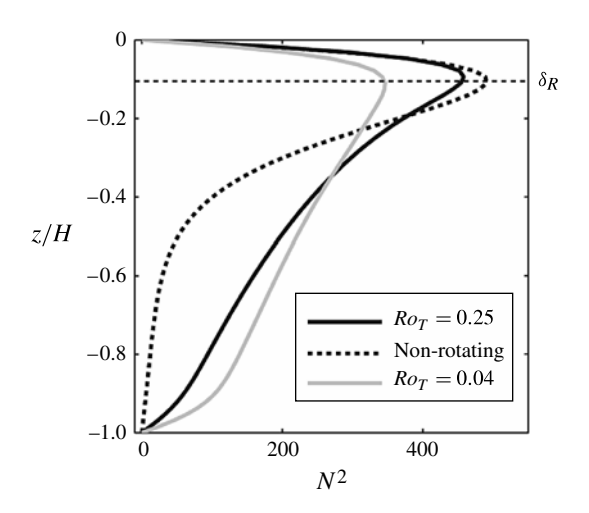


FIGURE 12. The horizontally averaged stratification normalized by  $(B_{max}/L_y^2)^{2/3}$  for simulations 14, 15 and 16 (Q=15,6 and 0, respectively). The horizontally dashed line represents Rossby's boundary layer scale (3.1) based on simulation 15 ( $Ra_B = 2 \times 10^{11}$ ).

## 6.2. The effects of $Ro_T$ on the stratification

Figure 12 shows a comparison between horizontally averaged stratification of two baroclinically active RHC simulations with different values of  $Ro_T$  (5.15) and the corresponding non-rotating HC one. In all cases the maximum stratification (thermocline depth) is at about  $z/H \sim -0.1$  which fits the scaling laws proposed by Rossby (3.1) better than the other suggested scaling laws (4.3), (4.4) (the corresponding boundary layer scale would be 1.5–4 times deeper depending on the value of Q). Clearly, deep stratification is increased for both of the RHC simulations. Note however, that the maximum in stratification is larger in magnitude

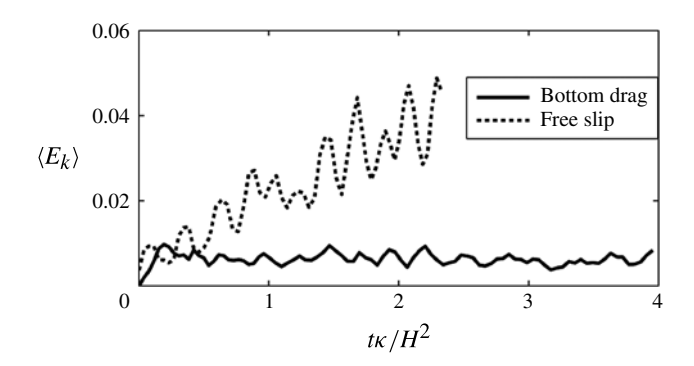


FIGURE 13. Volume-averaged kinetic energy (2.4a) normalized by  $(B_{max}L_y)^{2/3}$  for baroclinically active RHC simulations with (solid) and without (dash) bottom drag from simulations 12 and 13 (Q = 10).

for the baroclinically active RHC simulation with higher  $Ro_T$ . This difference is best demonstrated when comparing the ratio N/f in these two simulations. For the simulation with  $Ro_T = 0.04$ ,  $N/f \sim O(1)$  in the thermal boundary layer whereas in the simulation with  $Ro_T = 0.25$ ,  $N/f \sim O(10)$ . In the ocean typical values range between N/f = 20 and 50 in the thermocline and decreasing to N/f = 5 at depth (Marshall & Schott 1999). The above comparison demonstrates that the value of  $Ro_T$  affects the nature of the solution, particularly with respect to the stratification.

## 6.3. Steady state and bottom drag

Figure 13 shows a comparison between two baroclinically active RHC simulations, with the only difference being the inclusion of the bottom drag term of the form (2.6) in (2.1a). In contrast to the statistical steady state that is achieved in the simulation with bottom drag, there is a gradual increase in  $E_k$  for the simulation without bottom drag. In these baroclinically active simulations, energy can cascade to larger scales (Salmon 1980), and bottom drag is necessary to halt that inverse energy cascade (Vallis 2006). Traditionally the bottom drag r is a parametrization of the bottom Ekman layer and has a magnitude  $r \sim H^{-1} \sqrt{vf/2}$  (Vallis 2006). The wavenumber  $k_r$  at which the inverse energy cascade is halted scales like  $k_r \sim (r^3 \mathcal{E}^{-1})^{1/2}$ , where  $\mathcal{E}$  is the energy supply rate to the system. The Rossby deformation wavenumber  $k_d$  associated with a typical eddy length scale (Vallis 2006), can be estimated based on the rapidly rotating solution (5.11). Ideally the bottom drag magnitude should be chosen such that  $2\pi L_v^{-1} < k_r < k_d$ , in order to ensure that the baroclinic eddies do not grow and occupy the entire domain. For two-dimensional turbulence simulations  $k_r \approx (3\mathscr{B})^{3/2} (r^3 \mathscr{E}^{-1})^{1/2}$  with the constant  $\mathscr{B} = 5.8$  (Smith *et al.* 2002), so that  $(3\mathscr{B})^{3/2} \gg 1$ . In RHC the energy generation term at steady state  $\mathscr{E} = \kappa H^{-1} \Delta \hat{b} \leqslant B_{max}$ , so one can try to estimate  $k_r$  for these simulations. However, it is hard to accurately approximate  $\mathscr{B}$ in our three-dimensional, non-hydrostatic, Boussinesq simulations. We thus compared simulations of x-uniform RHC with a no-slip bottom boundary condition with those with bottom drag (not shown), and determined that the bottom drag magnitude that best parametrizes no-slip boundary conditions is  $r = 1.57H^{-1}\sqrt{vf/2}$ .

## 7. Energetics of RHC

Paparella & Young (2002) established a bound on the volume-averaged dissipation rate  $\epsilon \equiv \nu \langle || \nabla u ||^2 \rangle$  by combining the steady-state balance in (2.4*a*) and (2.4*b*) with no bottom drag (r = 0) to yield

$$\epsilon = \frac{\kappa}{H} \Delta \hat{b} \leqslant \frac{\kappa}{H} b_{max}. \tag{7.1}$$

With bottom drag, the left-hand side of (7.1) becomes  $\epsilon + \epsilon_d$ , where the dissipation due to bottom drag  $\epsilon_d \equiv \langle f_b(z) | \boldsymbol{u}_H |^2 \rangle$ . In all of the figures and discussion that follow in the next sections, although we computed  $\epsilon + \epsilon_d$  explicitly, we refer to it simply as  $\epsilon$  because in all of our baroclinically active RHC simulations  $\epsilon \gg \epsilon_d$ .

Using oceanic parameters defined in § 3,  $\kappa H^{-1}b_{max} = 1 \times 10^{-12} \text{ W kg}^{-1}$  for molecular diffusivity and  $1 \times 10^{-10} \text{ W kg}^{-1}$  for turbulent diffusivity. These values are 1–3 orders of magnitudes less than the observed values in the interior of the ocean,  $1 \times 10^{-9} \text{ W kg}^{-1}$ .

Winters & Young (2009) established a non-rigourous bound on the positive-definite term  $\Phi_d \equiv \kappa \langle (\mathrm{d}z_*/\mathrm{d}b) | \nabla b |^2 \rangle$ , defined by Winters *et al.* (1995) as the rate of change of the background potential energy  $E_b$  due to diabatic processes. At steady state, the balance in (2.4*c*) is

$$\Phi_d = \frac{\kappa}{H} z_*(\widehat{b_{top}}) \widehat{b_z}(0) \leqslant \kappa \frac{b_{max}}{\delta}. \tag{7.2}$$

Winters & Young (2009) estimated the thinnest possible scale upon which diabatic processes take place as  $\delta \sim Pr\kappa^{2/3}b_{max}^{-1/3}$ , leading to

$$\Phi_d \leqslant \frac{\kappa^{1/3} b_{max}^{4/3}}{Pr}.\tag{7.3}$$

The mixing efficiency in a Boussinesq flow is often defined as the ratio between the dissipation of  $E_a$  to that of the sum  $E_a + E_k$ , and is given by (Peltier & Caulfield 2003)

$$\gamma = \frac{\Phi_d - (\kappa/H)\Delta \hat{b}}{\Phi_d - (\kappa/H)\Delta \hat{b} + \epsilon}.$$
 (7.4)

At steady state, using (7.1) and (7.3),

$$\gamma \leqslant 1 - \frac{\delta}{H} = 1 - \frac{Pr^{2/3}}{Ra^{1/3}\alpha}.$$
 (7.5)

The bounds on  $\gamma$  and  $\Phi_d$ , may in fact be less restrictive, as pointed out by Scotti & White (2011). If, instead,  $\delta \sim \delta_R$ , the power in (7.3) and (7.5) should be reduced to 1/5. Note that for the boundary condition described in (2.2), the above bounds are only known *a posteriori*. Similar bounds can be established using the prescribed maximal buoyancy flux  $B_{max}$ . Finally, the above bounds assume nothing about the velocity boundary conditions and only require that the flow reaches a statistical steady state.

### 7.1. The mechanical energy cycles of RHC

Figure 14 shows a comparison between  $E_a$  (a),  $\epsilon$  (b),  $\Phi_d - \kappa H^{-1} \Delta \hat{b}$  (c) and  $\gamma$  (d), for non-rotating HC, x-uniform RHC and baroclinically active RHC. The amount of volume-averaged available potential energy increases five fold when rotation is introduced, but the increase is reduced when baroclinic instability is active.

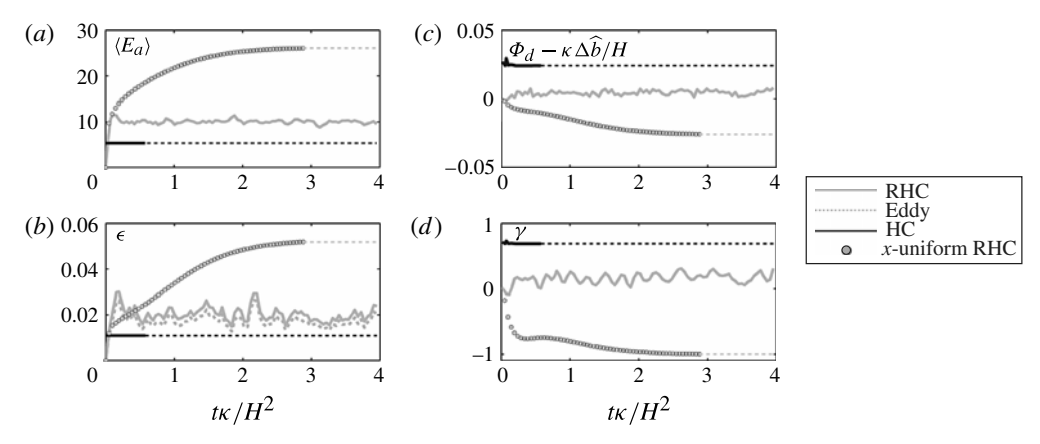


FIGURE 14. (a) Volume-averaged available potential energy (2.4d) normalized by  $(B_{max}L_y)^{2/3}$ , (b) volume-averaged kinetic energy dissipation  $\epsilon$  normalized by  $B_{max}$ , (c)  $\Phi_d - \kappa \Delta \hat{b}/H$  normalized by  $B_{max}$  and (d) the rate of dissipation of  $E_a$  to that of  $E_a + E_b$ ,  $\gamma$  (7.5), for non-rotating HC (simulation 1 – black), x-uniform RHC (simulation 9 – grey circles) and baroclinically active RHC (simulation 13 – grey). Horizontal dashed light grey and black lines are hypothesized extrapolations after equilibrium. The dashed grey line in (c) represents perturbations from x average (eddies).

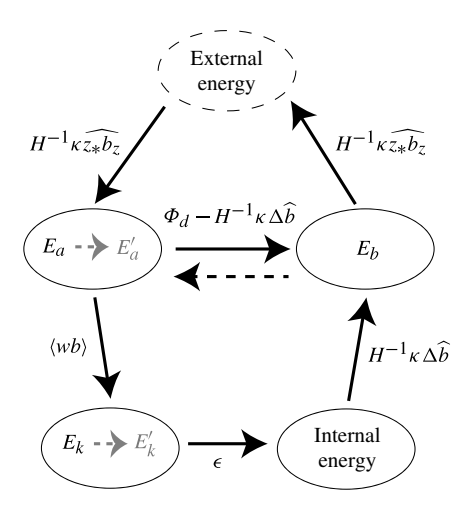


FIGURE 15. Energy cycle between mechanical, external and internal energies for statistically steady HC (adapted from Winters & Young 2009). The dashed black arrow indicates the sign reversal in  $\Phi_d - H^{-1}\kappa\,\Delta \widehat{b}$  for x-uniform RHC. The dashed grey arrows indicate that the kinetic and available potential energy reservoirs for baroclinically active RHC comprise mainly of eddy kinetic and available potential energies.

Nevertheless,  $\langle E_a \rangle$  values are still almost twice as large for baroclinically active RHC compared with non-rotating HC. The same is true for the volume-averaged dissipation, where the baroclinic eddies (dashed grey line in figure 14b) contribute much more to the dissipation than the x mean. Under the Boussinesq approximation with a linear equation of state (see Tailleux (2009) for a more general discussion) the difference  $\Phi_d - \kappa H^{-1} \Delta \hat{b}$  indicates the rate of conversion from  $E_a$  to  $E_b$  in these flows (see Winters & Young 2009 and figure 15). For fully developed stably stratified turbulent

flows  $\Phi_d \gg \kappa H^{-1} \Delta \hat{b} > 0$  so that most of the conversion is accomplished by mixing. In the present simulations  $\Phi_d - \kappa H^{-1} \Delta \hat{b}$  is positive for non-rotating HC, negative for x-uniform RHC, and positive again for baroclinically active RHC. The corresponding  $\gamma$  values are  $\sim 0.7$ ,  $\sim -1$  and  $\sim 0.17$ , respectively. The reason for the negative  $\gamma$  values in x-uniform RHC can be understood qualitatively by examining (7.5), and noting that  $\gamma < 0$  requires  $\delta > H$ , or no thermal boundary layer. Alternatively, note that  $\delta$  in (7.2), represents the scale at which diabatic processes take place. Because diffusion is the mechanism which fluxes heat laterally in this flow (figure 5), this suggests that  $\delta \sim L_{\gamma}$  and, consequently, that small aspect ratios ( $\alpha < 1$ ) can support negative  $\gamma$  values. In this case, viewing  $\gamma$  as the 'mixing efficiency' is misleading, because diabatic processes act on large scales, as opposed to the small scales which are often associated with mixing processes. Quantitatively we can use the rapidly rotating, analytical model described in § 5.1.1 to compute the different terms in (7.4) explicitly:

$$\frac{\kappa}{H} \Delta \widehat{b} = \frac{\kappa}{H} \left( \frac{1}{L_y L_x} \int_0^{L_y} \int_0^{L_x} \left( b_I(top) - b_I(bot) \right) \, \mathrm{d}y \, \mathrm{d}x \right) = \nu \left( \frac{\Gamma}{f} \right)^2, \qquad (7.6a)$$

$$\epsilon = \nu \left( \frac{1}{H L_y L_x} \int_0^{L_x} \int_0^{L_y} \int_0^0 \left( \frac{\partial u_I}{\partial z} \right)^2 \, \mathrm{d}x \, \mathrm{d}y \, \mathrm{d}z \right) = \nu \left( \frac{\Gamma}{f} \right)^2, \qquad (7.6b)$$

$$\Phi_d \approx \frac{1}{H L_y L_x} \int_0^{L_x} \int_0^{L_y} \int_{-H}^0 \frac{\kappa \left[ (\partial b_I / \partial y)^2 + (\partial b_I / \partial z)^2 \right]}{\mathrm{d}b / \mathrm{d}z_*} \, \mathrm{d}x \, \mathrm{d}y \, \mathrm{d}z = \kappa \alpha \left( \Gamma + Pr^2 \frac{\Gamma^3}{f^4} \right), \qquad (7.6c)$$

where  $db/dz_*$  was approximated using a linear profile

$$\frac{\mathrm{d}b}{\mathrm{d}z_{*}} \approx \frac{b_{I_{max}} - b_{I_{min}}}{H} = \Gamma \left( \frac{1}{\alpha} + Pr \frac{\Gamma}{f^{2}} \right) \approx \frac{\Gamma}{\alpha}. \tag{7.7}$$

The final simplification in (7.7) results from (5.13). As expected from a steady-state solution  $\kappa H^{-1}\Delta \hat{b} = \epsilon$  and thus  $\gamma = 1 - \kappa H^{-1}\Delta \hat{b}\Phi_d^{-1}$ . This ratio has to be greater than 1 for  $\gamma$  to be negative. Using (7.6) leads to

$$\frac{(\kappa/H)\Delta\widehat{b}}{\Phi_d} = \frac{\beta}{\alpha^2} + \frac{1}{\beta}.$$
 (7.8)

From (5.13)  $\beta^{-1} \gg 1$ . In order for  $\beta \alpha^{-2} \gg 1$ ,  $\alpha \ll Pr\Gamma/f^2$  which is satisfied in all of the numerical simulations as well as for typical oceanic parameters defined in § 3. If one scales  $\Gamma \sim b_{max}/L_y$  and from  $(\partial/\partial z)$  of (5.11),  $\partial b_I/\partial z = Pr(\Gamma/f)^2 \sim H^{-1}b_{max}$  then demanding that  $\alpha \ll Pr\Gamma/f^2$  is equivalent to requiring  $\alpha^2 \ll 1$ . This means that x-uniform RHC, with small aspect ratios is expected to yield negative  $\gamma$  values. Figure 15 shows the energy cycle of HC (Winters & Young 2009) along with the various energy transfer rates. The dashed black arrow shows the change to the lower cycle in the rapidly rotating regime when eddies are suppressed.

In baroclinically active RHC positive values of  $\Phi_d - \kappa H^{-1} \Delta \hat{b}$  indicate that the length scale at which diabatic processes take place is, as in non-rotating HC, much smaller than H so that a thermal boundary layer is again part of the solution and  $\gamma$  can again be viewed as the mixing efficiency. As a result the direction of the lower cycle in figure 15 is as was originally proposed by Winters & Young (2009). This demonstrates the importance of the eddies in the formation of the thermal boundary layer from an energetic point of view.

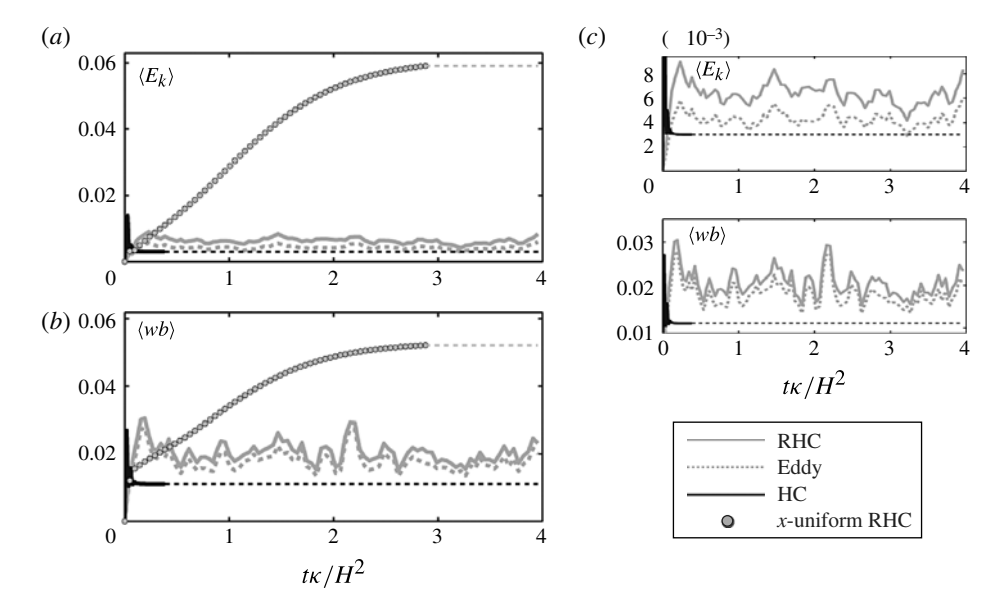


FIGURE 16. (a) Volume-averaged kinetic energy (2.4a) normalized by  $(B_{max}L_y)^{2/3}$  and (b) vertical buoyancy flux  $\langle wb \rangle$  normalized by  $B_{max}$ , for non-rotating HC (black), x-uniform RHC (grey circles) and baroclinically active RHC (grey). Horizontal dashed light grey and black lines are hypothesized extrapolations after equilibrium. Dashed grey lines represent perturbations from x average (eddies). (c) Comparison between non-rotating HC and baroclinically active RHC only. Simulations 1 (Q=0), 9 (Q=10) and 13 (Q=10).

Figure 16 shows a comparison between  $\langle E_k \rangle$  (a) and  $\langle wb \rangle$  (b), for non-rotating HC, x-uniform RHC and baroclinically active RHC. The volume averaged kinetic energy increases ten fold when rotation is introduced but the increase is somewhat reduced when baroclinic eddies are active. The same is true for  $\langle wb \rangle$  although the increase in the x-uniform case is not as large. In x-uniform RHC, the flow is primarily in the x direction, in fact 99% of  $\langle E_k \rangle$  is due to  $u^2/2$  (not shown). Figure 16(c) shows that baroclinically active RHC still has  $\langle E_k \rangle$  and  $\langle wb \rangle$  values two to three times larger than non-rotating HC. Furthermore it is evident that the contribution to both the vertical buoyancy flux and the kinetic energy is dominated by the eddies  $(w'b', E'_k)$ , as is the case for kinetic energy dissipation  $\epsilon'$  (figure 14c). This suggests that each individual term in the kinetic energy equation (2.4a) and the kinetic energy reservoir (grey shadow in figure 15) are dominated by the eddy field.

Figure 17 shows snapshots of horizontal slices taken at the base of the thermal boundary layer  $(z/H \sim -0.1)$  from a typical baroclinically active RHC simulation. Figure 17(a) shows the density field exhibiting eddying structures of different scales. Figure 17(b) shows the corresponding diabatic processes term  $\Phi_d$  (7.2) which is associated with diapycnal mixing. Note that areas of elevated mixing correspond well with the edges of the eddies and eddy filaments suggesting that eddies dominate the diabatic processes (mixing) in these flows. In a statistical steady state  $\Phi_d$  is balanced by the external energy term  $H^{-1}\kappa \widehat{z_*b_z}$  (2.4c) which supplies energy to the available potential energy ( $E_a$ ) reservoir (figure 15). The eddy dominance of  $\Phi_d$  and wb along with the statistical steady state balance in (2.4c) and the fact that  $\Phi_d > H^{-1}\kappa \Delta \widehat{b}$ 

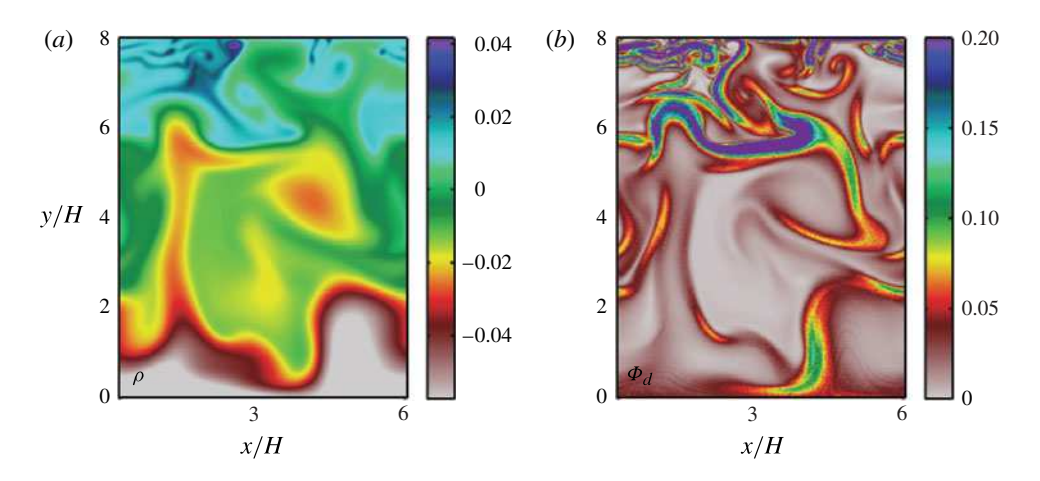


FIGURE 17. Snapshots of horizontal slices of (a) density normalized by  $HB_{max}\rho_0/g\kappa$  and (b) diapycnal mixing  $(\Phi_d)$  normalized by  $B_{max}$ , at  $z/H \sim -0.1$ . Simulation 14 (Q=15).

(figure 14c) suggest that each individual term in the  $E_a$  equation and the  $E_a$  reservoir are dominated by the eddy field as well.

## 8. Summary and discussion

Our main focus in this paper was to examine the effects of rotation on HC. In order to understand these effects with and without baroclinic instability, we have designed the RHC simulations in two steps. First, we analysed x-uniform RHC simulations, in which baroclinicity was suppressed (§ 5). Second, we examined simulations in which we allowed for baroclinic instability to ensue (§ 6). Our results show that rapid rotation and baroclinic instability greatly alter the steady state of non-rotating HC and thus are essential components of process-based models of the overturning circulation and thermal structure of the ocean.

In the moderately rotating regime ( $Q \sim O(1)$ ), the steady solution is very similar to the non-rotating solution, as was shown by the laboratory experiments of Hignett *et al.* (1981) and Park & Whitehead (1999). This solution supports a thin thermal boundary layer, a single overturning circulation cell, and weak abyssal stratification that are all well described by Rossby's scaling law (3.1).

In the rapidly rotating regime  $(Q \gg 1)$ , however, the *x*-uniform solutions support no thermal boundary layer, weaker overturning circulation and greater values of stratification  $(N^2)$  that extend throughout the entire domain depth. The full-depth penetrating plume that transports cold fluid laterally along the bottom boundary in the non-rotating case is arrested by about a distance  $R_d$  away from the wall in the rapidly rotating case, resulting in sloping isopycnals that occupy an extensive portion of the lateral domain. None of the previously suggested scaling laws (4.3), (4.4) accurately describe these solutions. An analytical model (§ 5.1) can very well predict the interior stratification, circulation and lateral buoyancy gradient as long as the lateral extent of a typical sloping isopycnal is smaller than the domain length (5.9). Two main insights are gained from the analytical model. First, the interior, 'eddy-less', lateral buoyancy gradient  $\partial b/\partial y$  is, to a good approximation, constant. Second, the non-dimensional number  $Ro_T$  (5.15) is important to the nature of the solution. Note that the analytical

model can easily be expanded to account for stress at the top and for different distributions of surface buoyancy flux.

The lateral buoyancy flux in the rapidly rotating, x-uniform solutions is dominated by diffusion and not advection, as was the case in the non-rotating and moderately rotating solutions. From an energetic point of view, this means that diffusion acts to build up available potential energy, resulting in negative values of  $\Phi_d - H^{-1}\kappa \Delta \hat{b}$  and  $\gamma$  (7.4). Increased values of  $E_a$  and  $\epsilon$  compared with non-rotating solutions indicate that rapid rotation enables the extraction of more available potential energy compared with non-rotating HC with the same buoyancy forcing. These x-uniform simulations, however, are unstable and are used here primarily to provide insight into the key features of the mean flow. Detailed linear stability analysis was carried out analytically for Pr = Ri > 1 (§ 5.1.2), in order to predict the horizontal scale of the most unstable mode. The transverse scale  $L_x \geqslant 10R_d$  was used in the baroclinically active simulations to allow the formation of enough eddies within the domain.

In the baroclinically active RHC solution a thermal boundary layer is again supported (compared with the x-uniform simulations), abyssal stratification is increased and multiple overturning cells are formed (compared with non-rotating simulations). Analyzing these solutions using a TEM framework shows the dominance of the eddy streamfunction in transporting buoyancy in these flows. The relative contribution of the mean flow is completely negligible. The interior eddy streamfunction is very well represented by the QG form  $\psi_{QG}^*$  (6.6), suggesting the isopycnal slope is small. Because the residual streamfunction contours intersect buoyancy contours throughout the interior of the flow the eddy buoyancy fluxes have a non-negligible diabatic component. This is in contrast to channel flows that are forced by surface stress (wind) as well as buoyancy fluxes (see for example Marshall & Radko 2003). A good measure of stratification in these flows is the ratio N/f. This ratio increases for increasing  $Ro_T$ . Note, that  $Ro_T$  can be expressed in terms of the other nondimensional numbers that govern this problem (specifically  $Ro_T \sim Ra^{1/5}Q^{-2}Pr^{-1}$ ). The solution dependence on  $Ro_T$  thus suggests that the ratio between the non-dimensional parameters that govern RHC is important in addition to their absolute magnitudes. Qualitatively, it appears that previously suggested scaling laws (4.3), (4.4) overestimate the thermal boundary layer depth in these flows.

The lateral buoyancy flux is dominated by eddy flux  $(\overline{v'b'})$ , where perturbations are from an x average. In terms of a TEM framework this means that buoyancy is predominantly 'advected' by the eddy velocity  $v^*$  (6.7). The kinetic and available potential energy reservoirs and the terms in the evolution (2.4a) and (2.4d) are dominated by the eddy field as well. The difference  $\Phi_d - H^{-1}\kappa \Delta \hat{b}$  is positive for baroclinically active RHC, demonstrating the importance of the eddies in mixing the fluid. The value of  $\gamma$ , which can now be interpreted as a mixing efficiency, is reduced from  $\sim$ 0.7 in non-rotating HC to  $\sim$ 0.17, a value similar to that commonly assumed in small-scale stratified turbulence and in the ocean. Although the energy bounds (7.1), (7.3), (7.5) hold, reaching a steady state is no longer independent of boundary conditions. Bottom drag (used to parametrize the bottom Ekman layer resulting from no-slip boundary conditions) is needed to allow the flow to equilibrate, at least over diffusive time scales  $(H^2/\kappa)$ .

The re-establishment of the thermal boundary layer in the baroclinically active simulation compared with the x-uniform ones suggests that the eddies play an important role in the thermal boundary layer formation. Eddies are responsible for most of the vertical and lateral buoyancy fluxes in the flow, overcoming the diffusive

dominance of the *x*-uniform simulations that do not support a thermal boundary layer. Furthermore, we hypothesize that it is the combined effect of the lateral transport of the eddies and the depth-dependent buoyancy of the negatively buoyant plume that set the deep stratification in this flow.

Because the kinetic and available potential energy are dominated by eddies ( $E_k \sim E_k'$ ,  $E_a \sim E_a'$ ), the mixing efficiency is close to values typically reported for actively turbulent flows, and bottom drag appears to be necessary to halt the inverse energy cascade and achieve a statistically steady state, the flow has the main characteristics of geostrophic turbulence. This observation does not contradict Paparella & Young's (2002) 'antiturbulence' theorem, which is based on a definition of three-dimensional turbulence consistent with a Kolmogorov inertial subrange. The geostrophically turbulent nature of baroclinically active RHC is a critical feature that distinguishes it from non-rotating HC and emphasizes the importance of rapid rotation in relating these process based models to the real ocean.

The importance of baroclinic eddies to the ocean's thermocline, stratification and overturning circulation is a concept well-studied by multiple authors in both laboratory experiments (Marshall *et al.* 2002) and numerical simulations using general circulation models (GCMs) of different resolutions and configurations (see, for example, Henning & Vallis 2004; Wolfe & Cessi 2010). The hydrostatic approximation and parametrization of convection via 'convective-adjustment', which are typical of GCMs, reduce the detail by which processes such as entrainment and mixing in the negatively buoyant plume can be represented. These processes are thought to be of great importance (Hughes, Hogg & Griffiths 2009; Stewart 2012).

The applicability of DNSs that resolve such processes (such as those described in this paper) to large-scale ocean dynamics is, however, open to question. The Ra number, aspect ratio and rotation rates (Q) presented here are nowhere near those observed in the ocean. Nevertheless, we argue that understanding physical mechanisms such as the combined effects of baroclinic eddies, the negatively buoyant plume and, in future work, mechanical forcing can lead to insights into oceanic processes.

#### Acknowledgements

Discussions with W. Young were much appreciated and gratefully acknowledged. We would like to thank C. Papadopoulos for continuous technical support which made this work possible. This work was supported by the National Science Foundation (grant number OCE-0926481).

# Appendix. Details of analytical solution described in § 5.1

The solution to (5.5) subject to no-slip boundary condition is

$$\tilde{\psi} = \frac{d^2 \Gamma}{2f} + d\Gamma [P1(z) + P2(z) + P3(z) + P4(z)], \tag{A 1}$$

where

$$P1(z) = \frac{d \cosh(H/d) \cosh(z/d) (\sec(H/d) \cos(z/d) - \coth(H/d) \sin((H+z)/d))}{2f (\sec(H/d) \cosh(H/d) - \sin(H/d) \cosh(H/d))},$$
 (A 2a)

$$P2(z) = \frac{d \sec(H/d) \cosh(H/d) \cosh(H/d) \cos(z/d) \sinh(z/d)}{2f (\sec(H/d) \cosh(H/d) - \sin(H/d) \csc(H/d))},$$
(A 2b)

$$P3(z) = -\frac{d\cos(z/d)\sinh(z/d)(\tan(H/d) + \coth(H/d))}{2f(\sec(H/d)\cosh(H/d) - \sin(H/d)\cosh(H/d))},$$
(A 2c)

$$P4(z) = \frac{d\cosh\left(z/d\right)\left(-\tan\left(H/d\right)\sin\left(z/d\right) + \sinh\left(H/d\right)\sin\left((H+z)/d\right) + \coth\left(H/d\right)\sin\left(z/d\right)\right)}{2f\left(\sec\left(H/d\right)\cosh\left(H/d\right) - \sin\left(H/d\right)\operatorname{csch}\left(H/d\right)\right)}.$$

(A 2d)

The corresponding lateral velocity  $\tilde{v}$  is

$$\tilde{v} = \Gamma [V1(z) + V2(z) + V3(z) + V4(z)], \tag{A3}$$

where:

$$V1(z) = \frac{d \sinh(z/d) (\sinh(H/d) \sin((H+z)/d) + 2 \coth(H/d) \sin(z/d))}{2f (\sec(H/d) \cosh(H/d) - \sin(H/d) \operatorname{csch}(H/d))},$$
(A 4a)

$$V2(z) = \frac{d \cosh(z/d) (\sinh(H/d) \cos((H+z)/d) - 2 \tan(H/d) \cos(z/d))}{2f (\sec(H/d) \cosh(H/d) - \sin(H/d) \csc((H/d))},$$
(A 4b)

$$V3(z) = -\frac{d\cosh{(H/d)}\sinh{(z/d)}\left(\coth{(H/d)}\left(\sin{((H+z)/d)} + \sec{(H/d)}\sin{(z/d)}\right) - \sec{(H/d)}\cos{(z/d)}\right)}{2f\left(\sec{(H/d)}\cosh{(H/d)} - \sin{(H/d)}\operatorname{csch}{(H/d)}\right)},$$
(A 4c)

$$V4(z) = -\frac{d\cosh\left(H/d\right)\cosh\left(z/d\right)\left(\sec\left(H/d\right)\sin\left(z/d\right) - \tan\left(H/d\right)\coth\left(H/d\right)\sin\left((H+z)/d\right)\right)}{2f\left(\sec\left(H/d\right)\cosh\left(H/d\right) - \sin\left(H/d\right)\operatorname{csch}\left(H/d\right)\right)}.$$
(A 4d)

The corresponding transverse velocity  $\tilde{u}$  is

$$\tilde{u}(z) = \frac{\Gamma}{f}(z + p_y^0) + \Gamma[U1(z) + U2(z) + U3(z) + U4(z)], \tag{A5}$$

where

$$U1(z) = -\frac{d\cosh\left(z/d\right)\left(\operatorname{csch}\left(H/d\right)\cos\left((H+z)/d\right) + \coth\left(H/d\right)\cos\left(z/d\right)\left(\operatorname{sec}\left(H/d\right)\cosh\left(H/d\right) - 2\right)\right)}{2f\left(\operatorname{sec}\left(H/d\right)\cosh\left(H/d\right) - \sin\left(H/d\right)\operatorname{csch}\left(H/d\right)\right)},$$

(A 6a)

$$U2(z) = -\frac{d \sec(H/d) \cosh(H/d) \sin(z/d) \cosh(z/d)}{2f \left(\sec(H/d) \cosh(H/d) - \sin(H/d) \operatorname{csch}(H/d)\right)},$$
(A 6b)

$$U3(z) = \frac{d \sinh(z/d) (2 \tan(H/d) \sin(z/d) - \sinh(H/d) \sin((H+z)/d))}{2f (\sec(H/d) \cosh(H/d) - \sin(H/d) \csc(H/d))},$$
(A 6c)

$$U4(z) = \frac{d\cosh\left(H/d\right)\sinh\left(z/d\right)\left(\tan\left(H/d\right)\coth\left(H/d\right)\cos\left((H+z)/d\right) - \sec\left(H/d\right)\cos\left(z/d\right)\right)}{2f\left(\sec\left(H/d\right)\cosh\left(H/d\right) - \sin\left(H/d\right)\operatorname{csch}\left(H/d\right)\right)},\tag{A 6d}$$

$$p_{y}^{0} = \left(\frac{d\left(\cos{(2H/d)} + \cosh{(2H/d)} - 2\cos{(H/d)}\cosh{(H/d)}\right)}{\sin{(2H/d)} - \sinh{(2H/d)}} + H\right),\tag{A 6}e)$$

and finally the corresponding buoyancy field b is

$$\tilde{b}(z) = \frac{\Gamma v}{\kappa f} \left( \tilde{u}(z) - \frac{\Gamma}{f} p_y^0 \right). \tag{A7}$$

Note that z has not been transformed as in the free-slip case and is in the interval [-H, 0]. Equation (5.7) still holds, leading to

$$\Gamma^3 \mathscr{H}_{ns_1} + \Gamma \kappa H = |\mathscr{F}_{1/2}|, \tag{A 8}$$

where  $\mathcal{H}_{ns} = H_{ns_1} + H_{ns_2} + H_{ns_3} + H_{ns_4} > 0$  and

$$H_{ns_{1}} = \frac{d^{4} \left(15d \sin \left(4H/d\right) - 8H \cos \left(4H/d\right) + 8H \sin \left(3H/d\right) \sinh \left(H/d\right) + 2 \cos \left(2H/d\right) \left(4H - 15d \sinh \left(2H/d\right)\right)\right)}{64f^{2} \kappa \left(\sin \left(2H/d\right) - \sinh \left(2H/d\right)\right)^{2}},$$
(A 9a)

 $H_{ns_{2}} = \frac{d^{4} \left(16 H \cos \left(H/d\right) \cosh \left(H/d\right) \cosh \left(2 H/d\right) + 2 \sin \left(2 H/d\right) \left(5 d \left(3 \cosh \left(2 H/d\right) + 2\right) - 28 H \sinh \left(2 H/d\right)\right)\right)}{64 f^{2} \kappa \left(\sin \left(2 H/d\right) - \sinh \left(2 H/d\right)\right)^{2}}$ 

(A9b)

$$H_{ns_3} = \frac{d^4 \cosh{(H/d)} \left(-35 d \sinh{(H/d)} - 8 \cos{(H/d)} \left(5 d \sin{(2H/d)} + H \cos{(2H/d)} - 5 d \sinh{(2H/d)}\right)\right)}{32 f^2 \kappa \left(\sin{(2H/d)} - \sinh{(2H/d)}\right)^2}, \quad \text{(A 9c)}$$

$$H_{ns_4} = \frac{d^4 \left(8 H \sin \left(H/d\right) \left(2 \sinh \left(H/d\right) + \sinh \left(3 H/d\right)\right) + 2 \sinh \left(H/d\right) \left(8 H \sinh \left(3 H/d\right) - 15 d \cosh \left(3 H/d\right)\right)\right)}{64 f^2 \kappa \left(\sin \left(2 H/d\right) - \sinh \left(2 H/d\right)\right)^2}.$$
(A 9d)

For free-slip bottom boundary condition the solution is (5.6), where

$$F_1(z') = \sin(z'/d)\cosh(z'/d), \qquad (A 10a)$$

$$F_2(z') = \cos(z'/d)\sinh(z'/d), \qquad (A 10b)$$

$$G_1 = \frac{d(\sin(H/2d))\sin(H/2d) - \cos(H/2d))\cos(H/2d)}{f(\cos(H/d)) + \cosh(H/d)},$$
 (A 10c)

$$G_2 = \frac{d(\sin(H/2d)\sinh(H/2d) + \cos(H/2d)\cosh(H/2d))}{f(\cos(H/d) + \cosh(H/d))}.$$
 (A 10d)

In (5.8),  $\mathcal{H}_{fs} = H_{fs_1} + H_{fs_2} + H_{fs_3} > 0$ , where

$$H_{fs_1} = \frac{d^4 \left( -d\sin(H/d) + H\cos(H/d) + H\cos(H/d) - d\cos(H/d) + 2\right)\sinh(H/d)}{4f^2 \kappa \left( \cos(H/d) + \cosh(H/d) \right)},$$
(A 11a)

$$H_{fs_1} = \frac{d^4 \left( -d\sin(H/d) + H\cos(H/d) + H\cos(H/d) - d\cos(H/d) + 2\right)\sinh(H/d)}{4f^2\kappa \left(\cos(H/d) + \cosh(H/d)\right)}, \qquad (A 11a)$$

$$H_{fs_2} = \frac{11d^5 \sin(2H/d) + d^4 \left( 4\cosh(H/d) \left( 5d\sin(H/d) + 2H\cos(H/d) \right) + 8H\right)}{128f^2\kappa \left(\cos(H/d) + \cosh(H/d)\right)^2}, \qquad (A 11b)$$

$$H_{fs_3} = \frac{d^5 \left(20 \cos \left(H/d\right) \sinh \left(H/d\right) - \left(\cos \left(2H/d\right) - 11\right) \sinh \left(2H/d\right) + \sin \left(2H/d\right) \left(-\cosh \left(2H/d\right)\right)\right)}{128 f^2 \kappa \left(\cos \left(H/d\right) + \cosh \left(H/d\right)\right)^2}.$$
(A 11c)

#### REFERENCES

- ANDREWS, D. G 1981 A note on potential energy density in a stratified incompressible fluid. J. Fluid Mech. 107, 227-236.
- ANDREWS, D. G. & MCINTYRE, M. E. 1976 Planetary waves in horizontal and vertical shear: the generalized Eliassen-Palm relation and the mean zonal acceleration. J. Atmos. Sci. 33, 2031-2048.
- ANDREWS, D. G. & McIntyre, M. E. 1978 Generalized Eliassen-Palm and Charney-Drazin theorems for waves on axisymmetric mean flows in compressible atmospheres. J. Atmos. Sci. **35**, 175–185.
- BEARDSLEY, R. C. & FESTA, J. F. 1972 A numerical model of convection driven by a surface stress and non-uniform horizontal heating. J. Phys. Oceanogr. 2 (4), 444–455.
- BRYAN, K. & COX, M. D. 1967 A numerical investigation of oceanic general circulation. Tellus 19,
- CESSI, P. & FANTINI, M. 2004 The eddy-driven thermocline. J. Phys. Oceanogr. 34, 2642–2658.
- CHIU-WEBSTER, S., HINCH, E. J. & LISTER, J. 2008 Very viscous horizontal convection. J. Fluid Mech. 611, 395-426.
- COMAN, M. A., GRIFFITHS, R. W. & HUGHES, G. O. 2006 Sandström's experiments revisited. J. Mar. Res. 64, 783-796.
- EADY, E. 1949 Long waves and cyclone waves. Tellus 1, 33-52.
- HAZEWINKEL, J., PAPARELLA, F. & YOUNG, W. R. 2012 Stressed horizontal convection. J. Fluid *Mech.* **692**, 317–331.
- HENNING, C. & VALLIS, G. K. 2004 The effects of mesoscale eddies on the main subtropical thermocline. J. Phys. Oceanogr. 34, 2428-2443.
- HIGNETT, P., IBBETSON, A. & KILLWORTH, P. D. 1981 On rotating thermal convection driven by non-uniform heating from below. J. Fluid Mech. 109, 161-187.

- HOLLIDAY, D. & MCINTYRE, ME 1981 On potential energy density in an incompressible stratified fluid. *J. Fluid Mech.* **107**, 221–225.
- HUGHES, G. O. & GRIFFITHS, R. W. 2008 Horizontal convection. *Annu. Rev. Fluid Mech.* 40, 185–208.
- HUGHES, G. O., HOGG, A. M. & GRIFFITHS, R. W. 2009 Available potential energy and irreversible mixing in the meridional overturning circulation. *J. Phys. Oceanogr.* 39, 3130–3146
- ILICAK, M. & VALLIS, G. K. 2012 Simulations and scaling of horizontal convection. *Tellus A* **64**, 18377.
- JEFFREYS, H. 1925 On fluid motions produced by differences of temperature and humidity. Q. J. R. Meteorol. Soc. 51, 347–356.
- KILLWORTH, P. D. & MANINS, P. C. 1980 A model of confined thermal convection driven by non-uniform heating from below. *J. Fluid Mech.* **98**, 587–607.
- KING, E. M., STELLMACH, S., NOIR, J., HANSEN, U. & AURNOU, J. M. 2009 Boundary layer control of rotating convection systems. *Nature* **457**, 301–304.
- MARSHALL, J., JONES, H., KARSTEN, R. & WARDLE, R. 2002 Can eddies set ocean stratification? J. Phys. Oceanogr. 32, 26–38.
- MARSHALL, J. & RADKO, T. 2003 Residual-mean solutions for the antarctic circumpolar current and its associated overturning circulation. *J. Phys. Oceanogr.* 33, 2341–2354.
- MARSHALL, J & SCHOTT, F. 1999 Open-ocean convection: observations, theory and models. *Rev. Geophys.* 37, 1–64.
- MOLEMAKER, M. J. & MCWILLIAMS, J. C. 2010 Local balance and cross-scale flux of available potential energy. *J. Fluid Mech.* **645**, 295–314.
- MULLARNEY, J. C., GRIFFITHS, R. W. & HUGHES, G. O. 2004 Convection driven by differential heating at a horizontal boundary. *J. Fluid Mech.* **516**, 181–209.
- Munk, W. H. & Wunsch, C. 1998 Abyssal recipes II: energetics of tidal and wind mixing. *Deep-Sea Res.* **45**, 1977–2010.
- PAPARELLA, F. & YOUNG, W. R. 2002 Horizontal convection is non-turbulent. J. Fluid Mech. 466, 205–14.
- PARK, Y. G. & WHITEHEAD, J. A. 1999 Rotating convection driven by differential bottom heating. *J. Phys. Oceanogr.* **29**, 1208–1220.
- Peltier, W. & Caulfield, C. 2003 Mixing efficiency in stratified shear flows. *Annu. Rev. Fluid Mech.* **35**, 135–167.
- PEREZ-PEREZ, E., READ, P. L. & MOROZ, I. M. 2010 Assessing eddy parameterization schemes in a differentially heated rotating annulus experiment. *Ocean Model.* 32, 118–131.
- PLUMB, R. A. & FERRARI, R. 2005 Transformed Eulerian-mean theory. Part I: nonquasigeostrophic theory for eddies on a zonal-mean flow. *J. Phys. Oceanogr.* **35**, 165–174.
- ROBINSON, A. & STOMMEL, H. 1959 The oceanic thermocline and the associated thermohaline circulation. *Tellus* 11, 295–308.
- ROSSBY, T. 1965 On thermal convection driven by non-uniform heating from below: an experimental study. *Deep-Sea Res.* **12**, 9–16.
- ROSSBY, T. 1998 Numerical experiments with a fluid heated non-uniformly from below. *Tellus* **50A**, 242–257.
- ROULLET, G. & KLEIN, P. 2009 Available potential energy diagnosis in a direct numerical simulation of rotating stratified turbulence. *J. Fluid Mech.* **624**, 45–55.
- SALMON, R. 1980 Baroclinic instability and geostrophic turbulence. *Geophys. Astrophys. Fluid Dyn.* **15**, 165–211.
- SANDSTRÖM, J. W. 1908 Dynamishce versuche mit merrwasser. *Ann. Hydrogr. Marit. Meteorol.* **36**, 6–23.
- SANDSTRÖM, J. W. 1916 Meteorologische studien im Schwedischen Hochgebirge. *Göteb. Kungl. Vetensk. Vitterh. Handl.* 17, 1–48.
- Scotti, A., Beardsley, R. & Butman, B. 2006 On the interpretation of energy and energy fluxes of nonlinear internal waves: an example from Massachusetts Bay. *J. Fluid Mech.* **561**, 103–112.
- SCOTTI, A. & WHITE, B. 2011 Is horizontal convection really non-turbulent? *Geophys. Res. Lett.* **38**, L21609.

- SMITH, K. S., BOCCALETTI, G., HENNINGS, C. C., MARINOV, I., TAM, C. Y., HELD, I. M. & VALLIS, G. K. 2002 Turbulent diffusion in the geostrophic inverse cascade. *J. Fluid Mech.* **469**, 13–48.
- SMITH, R. 1976 Longitudinal dispersion of a buoyant contaminant in a shallow channel. *J. Fluid Mech.* **78**, 677–688.
- STERN, M. E. 1975 Ocean Circulation Physics. Academic.
- STEWART, K. D. 2012 The effect of sills and mixing on the meridional overturning circulation. PhD thesis, Australian National University, 128 pp.
- STONE, P. H. 1966 On non-geostrophic baroclinic instability. J. Atmos. Sci. 23, 390-400.
- TAILLEUX, R. 2009 On the energetics of turbulent mixing, irreversible thermodynamics, Boussinesq models, and the ocean heat engine controversy. *J. Fluid Mech.* **638**, 339–382.
- Tailleux, R. & Rouleau, L. 2010 The effect of mechanical stirring on horizontal convecion. *Tellus* **62A**, 138–153.
- VALLIS, G. K. 2006 Atmospheric and Oceanic Fluid Dynamics. Cambridge University Press.
- WELANDER, P. 1971 The thermocline problem. Phil. Trans. R. Soc. Lond. A 270, 415-421.
- WINTERS, K. B., LOMBARD, P. N., RILEY, J. J. & D'ASARO, E. A. 1995 Available potential energy and mixing in density stratified fluids. *J. Fluid Mech.* 289, 115–128.
- WINTERS, K. B. & YOUNG, W. R. 2009 Available potential energy and buoyancy variance in horizontal convection. *J. Fluid Mech.* **629**, 221–230.
- WINTERS, K. B. & DE LA FUENTE, A. 2012 Modelling rotating stratified flows at laboratory-scale using spectrally-based DNS. *J. Oceangr. Mod.* 49–50, 47–59.
- WINTERS, K. B. & BARKAN, R. 2012 Available potential energy density for Boussinesq fluid flow. J. Fluid Mech. in press.
- WHITEHEAD, J. A. 1981 Laboratory models of circulation in shallow seas. *Phil. Trans. R. Soc. Lond.* A **302**, 583–595.
- WHITEHEAD, J. A. & WANG, W. 2008 A laboratory model of vertical ocean circulation driven by mixing. *J. Phys. Oceanogr.* **38**, 1091–1106.
- WOLFE, C. L. 2013 Approximations to the ocean's residual overturning circulation. *J. Oceangr. Mod.* (submitted).
- WOLFE, C. L. & CESSI, P. 2010 What sets the strength of the mid-depth stratification and overturning circulation in eddying ocean models? *J. Phys. Oceanogr.* 40, 1520–1538.
- WUNSCH, C. & FERRARI, R. 2004 Vertical mixing, energy, and the general circulation of the oceans. *Annu. Rev. Fluid Mech.* **36**, 281–314.